Arch Computat Methods Eng manuscript No.
(will be inserted by the editor)

Phase-field modeling of individual and collective cell migration

Adrian Moure[1] · **Hector Gomez**[1,2,3]

Received: date / Accepted: date

Abstract Cell motion is crucial in human health and development. Cells may migrate individually or in highly coordinated groups. Cell motion results from complex intra- and extra-cellular mechanochemical interactions. Computational models have become a powerful tool to shed light on the mechanisms that regulate cell migration. The phase-field method is an emerging modeling technique that permits a simple and direct formulation of the moving cell problem and the interaction between the cell and its environment. This paper intends to be a comprehensive review of phase-field models of individual and collective cell migration. We describe a numerical implementation, based on isogeometric analysis, which successfully deals with the challenges associated with phase-field problems. We present numerical simulations that illustrate the unique capabilities of the phase-field approach for cell migration. In particular, we show 2D and 3D simulations of individual cell migration in confined and fibrous environments that highlight the mechanochemical interplay between the cell and the extracellular environment. We also show 2D simulations of cell co-attraction in non-confluent multicellular systems, in which the use of the phase-field method is crucial to capture the dynamics of the multicellular system.

email: Adrian Moure
amourero@purdue.edu

[1] School of Mechanical Engineering, Purdue University, 585 Purdue Mall, West Lafayette, IN 47907, USA

[2] Weldon School of Biomedical Engineering, Purdue University, 206 S Martin Jischke Dr, West Lafayette, IN 47907, USA

[3] Purdue University Center for Cancer Research, Purdue University, 201 S University St, West Lafayette, IN 47906, USA

1 Introduction

Cell motion occurs in many biological processes essential for life. While some cells move in a liquid medium by using cilia or flagella, most eukaryotic cells in the human body move through solid environments such as, e.g., the extracellular matrix or the basal lamina. Here we focus on the latter kind of cell migration. Thus, by cell migration we will refer to the crawling motion of cells on solid media. Cell migration is a highly coordinated process that results from complex interactions between the constituents of the cellular motile machinery and the extracellular environment. Cell motion manifests as individual motile cells or organized groups of cells that move as functional units. Both individual and collective cell migration regulate key biological functions such as tissue formation, wound healing, or cancer metastasis. Therefore, the biomechanics of cell migration has been, and continues to be, an active field of research.

Computational modeling of cell migration is an emerging field in biomechanics and biophysics. Computational models can overcome the intrinsic limitations of the experimental setups and help to further understand the mechanisms involved in cell migration. Likewise, the models can suggest new hypotheses to be tested in experiments. The biomechanical interactions between the intra- and extra-cellular agents are usually described through dynamic equations, coupled to a momentum balance law that accounts for the forces driving cell motion. A motile cell is an outstanding example of a moving boundary problem. Most of the challenges related to the numerical solution of moving boundary problems can be bypassed by using the phase-field method. The phase-field method is a modeling technique whose main advantage is the reformulation of a moving-boundary problem on a fixed domain. The phase-field method has become a prominent

approach to model problems with moving interfaces, such as cell motion.

In this paper, we review phase-field models of individual and collective cell migration. The paper is organized as follows: In Sect. 2 we provide a biological background to understand the mechanisms that produce cell motion. Section 3 reviews the state of the art of phase-field modeling of cell migration. In Sect. 4 we describe numerical methods used to solve the phase-field models, where we highlight a formulation based on isogeometric analysis. In Sect. 5 we show several 2D numerical examples of individual and collective cell migration, as well as a 3D example of individual cell migration in a fibrous environment. We finalize with the conclusions in Sect. 6.

2 Biomechanics of cell migration

At the beginning of this section, we provide a biological description of the eukaryotic cell. Then, we introduce the extracellular and intracellular elements involved in cell migration. Finally, we explain the mechanisms that produce cell motion and we indicate the different kinds of cell migration.

2.1 The eukaryotic cell

Eukaryotic cells (see Fig. 1) can be distinguished from other types of cells by their nucleus, a membrane-enclosed intracellular compartment where DNA is kept. Eukaryotic cells have other intracellular compartments that carry out diverse metabolic functions and a cytoskeleton that organizes the compartments, provides support, and drives cell motion.

Proteins. Proteins are the principal catalysts for most of the chemical reactions occurring in the cell. Proteins [5] are composed of modular units, called domains, which display a globular shape and contain from 40 to 350 amino acids. Proteins are in charge of diverse cellular functions, such as, e.g., generation of mechanical forces, the selective transport of molecules across the cell membrane, or the regulation of cellular processes. All these functions are accomplished by protein shape changes induced by ligand-binding events.

The cell membrane. The cell membrane consists of a continuous double layer of amphiphilic[1] lipid molecules that create closed compartments. The lipid bilayer behaves as a fluid in the in-plane direction and as a solid in the out-of-plane direction. In the in-plane direction, individual lipid molecules diffuse rapidly within their own monolayer. Membrane proteins, which are embedded in the lipid bilayer (see inset 1 in Fig. 1), are responsible for most of the membrane functions (e.g., signal transduction or cell-cell adhesion). Membrane proteins can diffuse throughout the membrane. However, cells have mechanisms to localize specific membrane proteins to certain regions of the membrane, causing the polarization of the cell (see Sect. 2.3).

[1] The lipid molecules possess one end with hydrophilic properties and the other end with hydrophobic properties.

Cytoplasm, cytosol, and organelles. Though there is controversy about this nomenclature, we will consider that the cytoplasm comprises the cytosol and the organelles (see Fig. 1). The cytosol, located in the cell's interior, is a complex mixture of ions, small molecules, and large water-soluble molecules such as proteins dissolved in water [5]. The eukaryotic cell is subdivided into functionally distinct membrane-enclosed compartments, or organelles, which display different structural organizations. On average, the membrane-enclosed compartments together occupy nearly half the volume of the cell, while the cytosol constitutes the other half. The cytoskeleton is a cellular scaffolding or skeleton that plays important roles in, e.g., intracellular transport, cellular division, or cell motility. We analyze the properties of the cytoskeleton in Sect. 2.2.

Cellular organization and body tissues. Tissue is a cellular organizational level intermediate between cells and organs. A tissue is an aggregate of similar cells that have the same origin and develop a specific function. Animal tissues can be grouped into four types, namely, (1) connective tissue, which supports, connects, and separates different types of tissues and organs of the body; (2) nervous tissue; (3) muscle tissue; and (4) epithelial tissue, which lines the cavities and surfaces of the structures throughout the body.

2.2 Constituents of cell motility

2.2.1 Cytoskeleton

The cytoplasm of the cell is spatially organized by a network of protein filaments known as the cytoskeleton [5]. The cytoskeleton also develops an active role in processes such as cell division, cell polarity, cell motility, and cellular shaping. The cytoskeleton is composed of three types of filaments (see Fig. 1):

Actin filaments. Two-stranded helical polymers comprised by the protein actin. Actin filaments are flexible structures which may be organized into a variety of linear bundles, two-dimensional networks, and three-dimensional gels.

Microtubules. Long and hollow cylinders made of the protein tubulin. They are usually organized with one end attached to a single microtubule-organizing center, called centrosome.

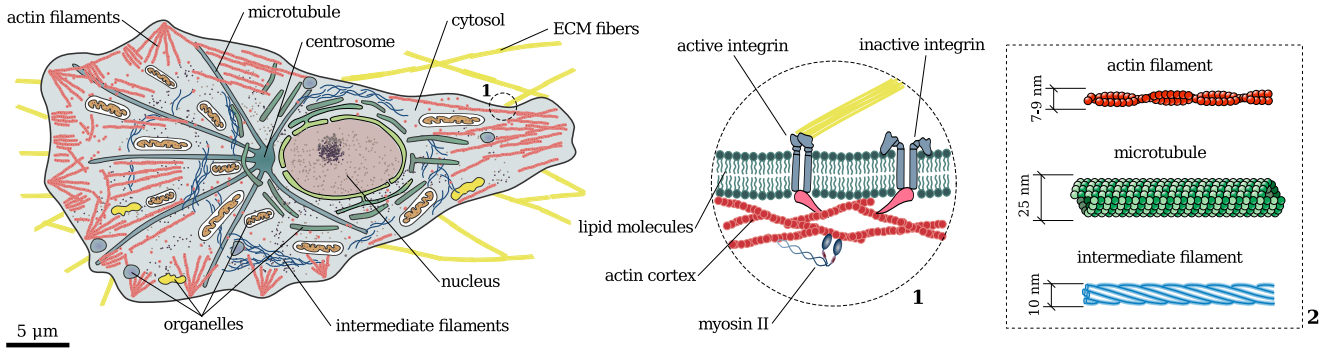

Fig. 1 Schematic representation of an eukaryotic cell. Inset 1 shows a detailed view of the cell membrane. Inset 2 shows the cytoskeleton filaments. (Adapted from [5])

Intermediate filaments. Rope-like fibers made of intermediate filament proteins. Intermediate filaments constitute a large and heterogeneous family of proteins in charge of different functions (e.g., mechanical strength or span cell junctions).

Compared to microtubules and intermediate filaments, actin filaments play a prime role in cell migration. Henceforth, we focus on actin filaments (F-actin), which are made up of smaller compact and globular subunits (G-actin). While F-actin forms a network that spreads throughout the cell, G-actin can diffuse rapidly within the cytosol. Cells are able to undergo rapid structural reorganizations by disassembling filaments at certain regions of the cell and reassembling new filaments in other regions. The process in which G-actin assemble into F-actin is called polymerization.

2.2.2 Accessory proteins

By accessory proteins we refer to hundreds of proteins that regulate the spatial organization and the dynamic behavior of the filaments and the subunits by binding to them. The response of these cytoskeleton-associated proteins is dictated by extracellular and intracellular signals. These accessory proteins are able to change the kinetics and determine the location of filament assembly and disassembly, or establish the kind of structure created by the filament network. Examples of accessory proteins are the pro-nucleation Arp2/3 complex, formin, and profilin, the destabilizing cofilin, or the gel-forming filamin and spectrin.

2.2.3 Molecular motors

Molecular motors are a type of proteins with the ability to bind to a filament and move steadily along it. The main functions of the molecular motors are the displacement of organelles within the cell and the cytoskeleton contraction involved in cell motion. Here, we focus on the myosin family, in particular, on myosin II, which binds to F-actin. Myosin II is composed of two heavy chains (see inset 1 in Fig. 1), each one with a globular head domain followed by a very long amino acid sequence. The myosin head, which moves along the actin filament, contains the force-generating machinery. On the other hand, the tail forms a long coiled-coil that may bundle with the tails of other myosin molecules. Myosin II achieves movement from the energy derived from repeated cycles of ATP hydrolysis[2] (more details in [5]). The contraction of the filament network is achieved by pairs of myosin with attached tails and heads bound to different filaments.

2.2.4 Basal lamina and extracellular matrix

The basal lamina is a layer of the extracellular matrix secreted by epithelial cells. The basal lamina separates the epithelium from the underlying connective tissue, and also constitutes the mechanical connection between them; see Fig. 2. The basal lamina works as a selective filter, establishes cell polarity, influences the cell metabolism, promotes cell survival, proliferation, differentiation, and is the substrate where cells migrate. The basal lamina is mostly composed of fibrous proteins (laminin, collagen IV, nidogen and perlecan).

The extracellular matrix (ECM) is an intricate network of macromolecules assembled into an organized mesh. The main component of the ECM is glycosaminoglycn, which usually creates a highly hydrated gel-like substance where the fibrous proteins are embedded. The gel provides resistance to compressive forces and also permits the rapid diffusion of nutrients through the network. The main fibrous proteins that comprise the ECM are collagen, elastin, and fibronectin (see [5] for further details). The ECM not only serves as a medium for migration, but also has direct consequences on the shape, polarity, and mode of migration of the cells (see Sect. 2.3).

[2] ATP hydrolysis is a molecular reaction that produces mechanical energy from chemical energy.

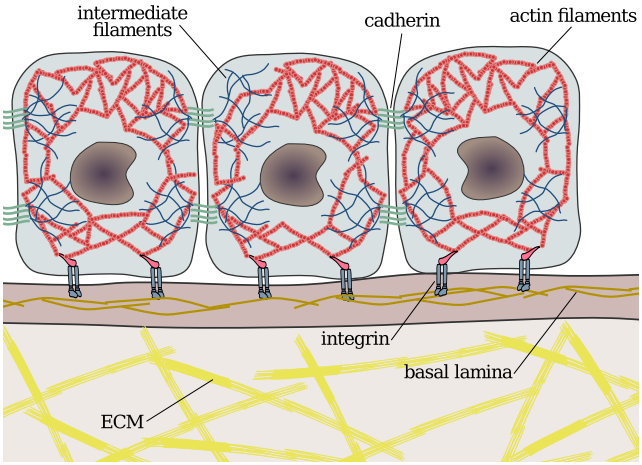

Fig. 2 Basal lamina and extracellular matrix (ECM). The basal lamina separates the epithelium from the underlying connective tissue. Cadherins mediate cell-cell adhesion. Integrins mediate cell-ECM adhesion.

2.2.5 Adhesion proteins

Cell-cell and cell-ECM junctions are diverse and develop functions such as signal transduction across the cell membrane, mechanical connection to other cells or the environment, or the tight sealing between cells in epithelia. Cadherin and integrin are two superfamilies that play a prominent role in cell migration (represented schematically in Fig. 2).

Cadherin and cell-cell adhesion. Cadherin is in charge of cell-cell adhesion and mediates symmetric junctions (i.e., cadherin binds to other cadherin). Strong connections are achieved by the formation of many individual bonds in parallel. Cadherins attach to the cytoskeleton filaments by means of a cluster of accessory proteins that connect the tail of the cadherin to the filament. Cadherins play a crucial role in tissue segregation, tissue formation, contact guidance, and chemotaxis.

Integrin and cell-ECM adhesion. Integrin is the main family of cellular adhesion receptors and is able to bind to most ECM proteins. Integrin develops both the anchoring and the signaling functions. Intregrin binds to laminin or fibronectin outside the cell, and to a complex of proteins connected to the cytoskeleton inside the cell. In case of integrin-actin filament connection, the main compounds of the cluster are talin and vinculin. Integrin may be found in an active or an inactive state (see inset 1 in Fig. 1). Only active integrins can conduct the connection. Integrin activation can be caused by an extracellular ligand that binds to integrin, or by intracellular regulatory molecules that activate talin, and consequently, integrin. Integrin activation usually constitutes the response to signals generated by other cells or the cell itself. The crosstalk between these signaling pathways permits complex interactions between the cell and its physical and chemical environment.

2.2.6 Actin cortex

The actin cortex is a thin network composed of actin filaments, myosin motors, and actin-binding proteins that lies directly beneath the plasma membrane [50]; see Fig. 1. The actomyosin cortex is attached to the cell membrane and may modify the properties of the membrane (e.g., the surface tension) by inducing stresses. Changes in the mechanical properties of the cortex are involved in cellular processes such as, e.g., cell division, tissue morphogenesis, and cell migration.

2.2.7 Membrane receptors

Membrane receptors are transmembrane proteins that mediate the communication between cells and their environment. They also undergo complex interactions with other membrane proteins such as integrin or cadherin. Receptors detect extracellular signals (e.g., an extracellular ligand that binds to the receptor) and trigger intracellular signal transduction pathways that control the cellular response to those signals. Receptors are key elements in the migration of cells directed by external signals.

2.2.8 Proteases

By proteases we refer to any kind of enzyme that is able to perform proteolysis, i.e., the breakdown of proteins into smaller amino acids. The most important proteases involved in ECM degradation are matrix metalloproteases (MMPs). As we describe in Sect. 2.3, MMPs have an outstanding role in cell migration, since they modulate the extracellular microenvironment providing new escape routes for the cells.

2.3 Cell migration

2.3.1 Molecular mechanisms

Cell migration is a multistep process that involves the integration and coordination of complex biochemomechanical signals. Cell motion can be initiated by chemical and physical factors in the cell environment, although some cells can undergo spontaneous migration. Individual cell migration is explained by the five-step model [71] plotted in Fig. 3. The closely coordinated steps of the model are the following:

1. **Protrusion of the leading edge.** Actin filaments assemble at the leading edge and push the cell membrane outwards. Different kinds of protrusive structures may be

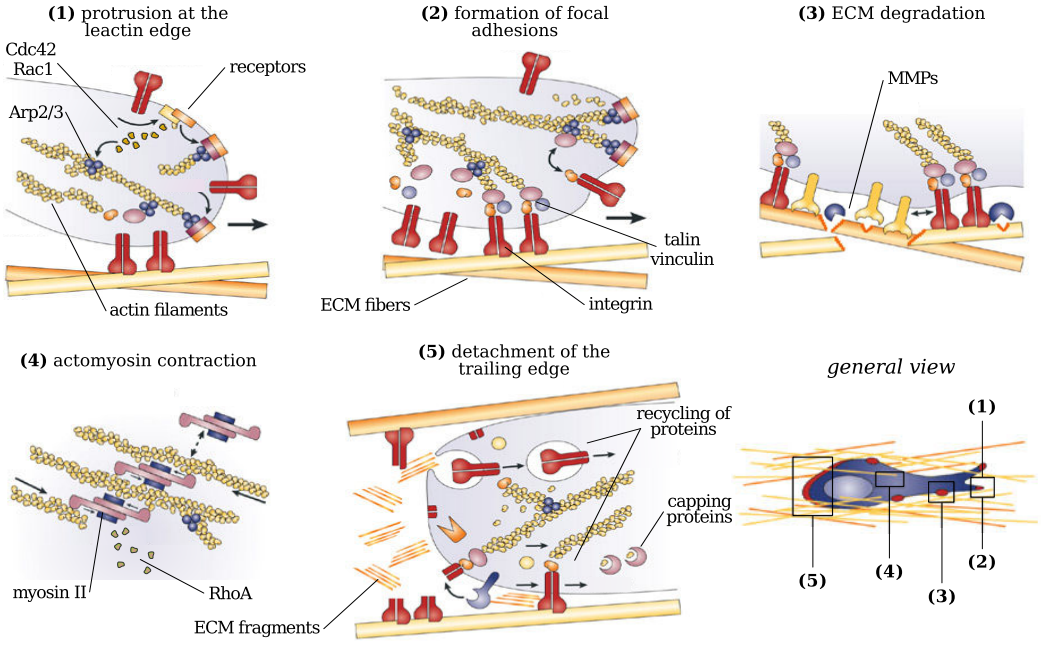

Fig. 3 Five-step model of cell migration. The steps are closely coordinated and correspond to cell motion through the ECM. In case of migration on a planar surface (e.g., the basal lamina) the steps are analogous with the exception of ECM degration, which does not occur. (Adapted from [71])

generated: filopodia (1D protrusions), lamellipodia (2D structures), or pseudopodia (3D protrusions). Cell protrusion is the result of the polymerization of F-actin underneath the membrane.

2. **Cell-matrix interaction and formation of focal contacts.** Integrins bind to ECM ligands at the leading edge of the cell, followed by the clustering of integrins and the recruitment of signaling proteins. This process leads to the formation of focal adhesions (multiprotein structures that regulate the cell response). Focal adhesions transmit forces to the environment and regulate cell motility through different signaling pathways.
3. **ECM degradation.** Proteolysis of the ECM by recruitment of surface proteases. ECM degradation is likely to provide the space required for cell expansion and migration.
4. **Cell contraction by actomyosin.** Myosin II binds to actin filaments forming a network known as actomyosin network. This network undergoes contraction, mainly located at the rear and central part of the cell. The forces generated by myosin are transmitted through the actin network to the surrounding environment (the substrate in the case of 2D migration).
5. **Detachment of the trailing edge.** Focal contacts disassemble at the trailing edge, while the cell's front is tightly attached. Thus, the actomyosin contraction produces the displacement of the cell body towards the leading edge.

These five points can be coordinated in many ways. The most common way (the morphological variants of cell migration are described in Sect. 2.3.3) involves the extension of F-actin structures that attach to the ECM via integrin molecules. Integrins cluster and develop a small focal complex that may grow, stabilize, and form a focal adhesion. Focal adhesions may induce the recruitment of proteases that degrade the ECM, which facilitates the extension of protrusions at the cell's front. At the same time, the actomyosin network undergoes contraction at the cell's body. Overall, the extension of protrusions at the cell's front and the retraction of the cell's back cause the motion of the cell.

2.3.2 Regulation of cell motion

The cellular response to temporal and spatial gradients of extracellular signals causes specific molecular events in different regions of the cell. The spatially distinctive molecular accumulation inside the cells, usually a front-back distinction, is known as *cell polarity* [145]. Significant progress [58, 176, 188] has been made to uncover the interactions between the different signaling pathways, also known as modules. The modules can be classified according to their main compounds, namely, phosphoinositides (PIs), their phosphatases, and Rho GTPases. Let us focus on the Rho GTPases [134] to illustrate the mechanisms of cell motility regulation. The main members of the Rho GTPases family are the Cdc42, Rac1, and RhoA proteins. Rho proteins are evenly distributed

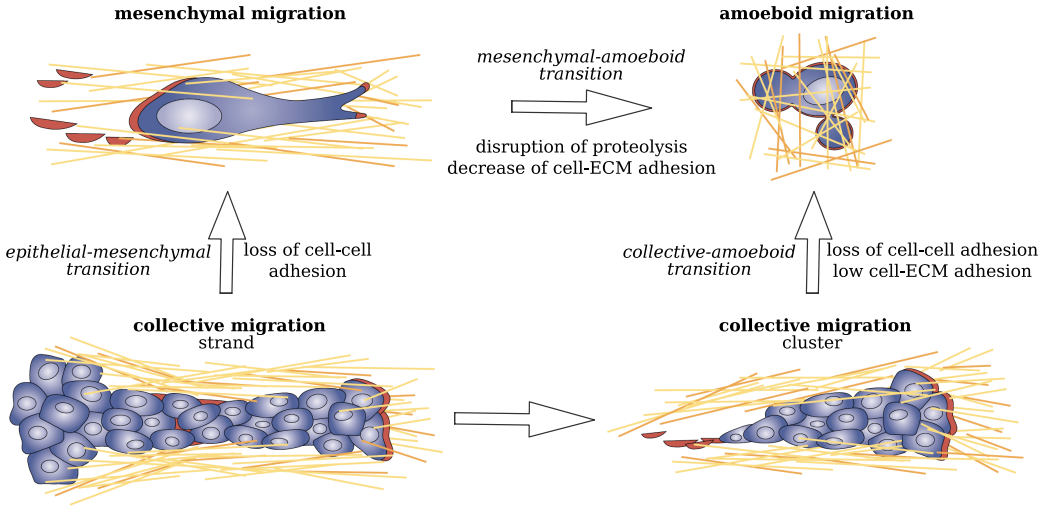

Fig. 4 Different modes of individual and collective cell migration. Cells can undergo transitions between different modes of migration. A transition implies an adaptive response to changes in the factors that control the modes of migration. We have indicated the main transitions observed in cell motility. Note that transitions are bidirectional processes (not indicated in the figure). (Adapted from [71])

in a resting and unpolarized cell. When the cell receives a signal that induces motion, Rho proteins reorganize spatially, such that Cdc42 and Rac1 are located at the cell's front (promoting actin polymerization) and RhoA at the cell's back (promoting contraction and F-actin bundling). These proteins can transition between a membrane-bound state and a cytosolic state, which permits a rapid diffusion throughout the cell. The activation of these proteins is initiated by members of their own module or another module, and is usually originated upstream in the signaling pathway by activated membrane receptors. The activation may be caused by chemical or mechanical (through the process known as mechanotransduction) stimuli. The mechanisms of cell regulation vary depending on the cell type and the mode of migration displayed by the cell.

Directed motion. An outstanding feature of motile cells is their ability to perceive external stimuli that can direct their motion, usually sensed by membrane proteins. The most common types of directed cell motion are: (1) Chemotaxis, induced by chemical cues, i.e., extracellular ligands that bind to the membrane receptors generating a chemotactic response through different signaling pathways; (2) Haptotaxis, driven by a gradient of cellular adhesion sites in the ECM or substrate [19]; (3) Durotaxis, caused by variations in the rigidity of the substrate (cells usually migrate to stiffer substrates because they can support stronger forces); (4) Others, such as electrotaxis [54], or tensotaxis [34].

2.3.3 Diversity in cell migration

Cell migration may be classified as individual or collective migration [72]. Both individual and collective migration display different morphological variants based, among other factors, on the cell type, the level of integrin engagement, the predominant cytoskeleton structure, and the production of proteases. The morphological variants are denoted as *modes of cell migration* (see Fig. 4). We list here some representative examples of cell migration modes:

- **Mesenchymal migration.** Individual cell migration with high levels of cell-ECM adhesion, cytoskeleton contractility, and ECM degradation. Mesenchymal cells follow the five-step model explained above and usually display a fibroblast-like shape.
- **Amoeboid migration.** Individual migration of elongated cells that translocate via rapid extensions and retractions of the membrane caused by dynamic actin-rich structures. Amoeboid cells usually lack stress fibers, focalized proteolytic activity, and mature focal adhesions. Cell movement is achieved by squeezing through the gaps between the ECM fibers.
- **Blebbing migration.** Individual cell migration similar to amoeboid motion where the membrane extensions are caused by blebs. Blebs [47] are rounded protrusions of the membrane caused by the increase of the intracellular cytosolic pressure along with the disruption of the membrane-actin cortex connection.
- **Chain migration.** It is not considered a collective, but a multicellular mode of migration where cells stream one after another in a strand-like fashion. The strand is generated by the first invading cell, while the rest of the cells transiently form and disrupt cell-cell contacts.
- **Collective migration.** The cytoskeletons of different cells are connected via cell-cell adhesions, which leads to a large and multicellular body moving as a functional unit.

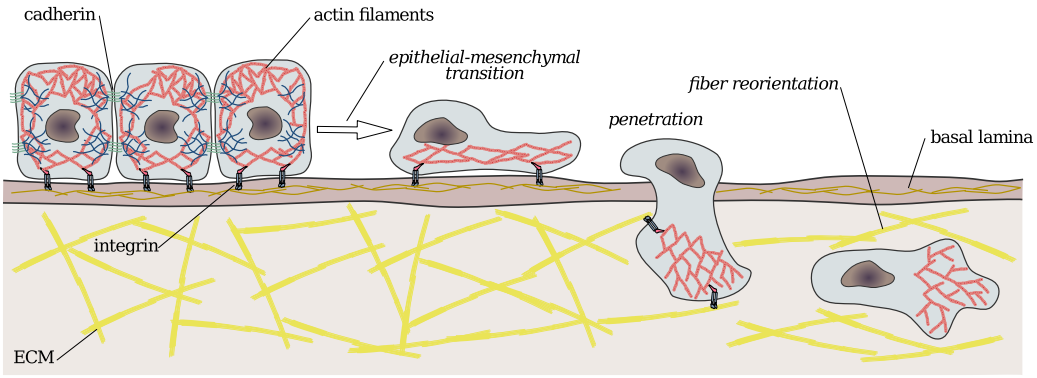

Fig. 5 Ephitelial-mesenchymal transition. Epithelial cells lose cell-cell adhesion and undergo the epithelial-mesenchymal transition. Mesenchymal migration in the ECM causes fiber degradation and reorientation.

The common configuration of the body consists of a group of highly motile cells located at the front which produce the migratory traction, while the inner and trailing cells are passively dragged behind (although in some cases, the inner cells are the ones that generate the active motile forces [184]). Depending on whether the group of moving cells detaches from the original tissue or not, we would refer to the group as a *strand* (the protruding body maintains contact with its original location) or a *cluster* (the group of cells is detached).

2.3.4 Plasticity of cell migration

Each cell type displays a particular *default* mode of migration. If any of the factors that determine the mode of migration is altered (e.g., ECM fiber density, orientation, stiffness, cell-cell adhesion, cell-ECM adhesion, or protease production), the cell could stop. However, cells may modify their migration mode showing an adaptive response, known as plasticity [177]. The cells may alter the mode of migration as an escape strategy in a process known as *transition*. The main transitions involved in cell invasion (some of them are shown in Fig. 4) are the following:

Epithelial-Mesenchymal Transition (EMT). An epithelial cell undergoes multiple biochemical changes that make the cell acquire a mesenchymal phenotype [180]. EMT involves the loss of the epithelial cell polarity, the detachment from the basal lamina, and the loss of cell-cell adhesion, which is regulated by E-cadherins. The emerging proteolytic activity produces the rupture of the basal lamina, which enable the penetration of the cells. Finally, the cell acquires a mesenchymal phenotype and initiates its migration, as shown in Fig. 5. The proteolytic activity takes place in the neighborhood of the leading edge. Instead of a complete breakdown, the fibers of the ECM are reoriented parallel to the direction of the cell's motion.

Mesenchymal-Amoeboid Transition (MAT). Cells transition from a mesenchymal to an amoeboid phenotype. MAT produces changes in the cell's morphology, the distribution of integrins, and the organization of the actin cytoskeleton. MAT may be caused by the disruption of proteolysis, a decrease of cell-ECM adhesion, or the inhibition of RhoA activity.

Collective-Amoeboid Transition (CAT). CAT is a transition similar to EMT. In a CAT, after the disruption of cell-cell adhesion and the detachment from the multicellular body, the cell displays integrin-independent amoeboid migration.

Mesenchymal-Epithelial Transition (MET). Plasticity of motile cells may occur in a bidirectional way. Both transitions from amoeboid to collective and amoeboid to mesenchymal have been observed. A common case is the MET, which involves the same molecular processes described for EMT in the opposite direction.

2.3.5 Singularities of collective cell migration

Collective migration is not only the result of many individual moving cells. On the contrary, collective motion displays a coordinate behavior not observed in individual cells, in which cell-cell adhesion and cell-cell communication play a crucial role. The intercellular junctions, mediated by cadherins, originate a particular type of actin cortex, which is connected to the cortex of the neighboring cells. The connection conducts force transmission and transforms the multicellular system into a contractile body that moves as a functional unit. The coordinate behavior observed in collective motion also requires intercellular communication. For instance, cell-cell communication promotes chemotaxis of cell clusters in shallow gradients of chemoattractant, where individual cells cannot chemotax effectively [120, 179]. Cell clusters also increase their motility by releasing a chemokine[3]

[3] Chemokines are signaling proteins secreted by the cells.

that creates a pericellular gradient. The chemokine gradient keeps the cluster packed and guides the cells behind the leading edge in the same direction as the leading cells [177]. The cooperative behavior is also observed in the cluster mechanics. It has been largely assumed that the cells located at the cluster's front (also known as the leaders) generate the motile forces, while the cells behind the leaders (known as the followers) are just passively dragged. A similar behavior was observed in [153], where the leaders are polarized but not the followers. Apart from force generation, leader cells also conduct ECM degradation and chemokine secretion, which proves the pivotal role of the leaders in collective migration. However, recent research has shown some cases in which follower cells push the leaders [184], suggesting that the tug-of-war between leaders and followers is more complex. The morphodynamics of multicellular systems is also determined by other factors such as the cell type, the pericellular proteolytic activity, or the properties of the extracellular environment. Although most experimental studies of collective motion focus on 2D monolayers (by means of the scratch-wound assay [151]), collective migration also manifests as 3D strands, multilayered bodies, or non-confluent clusters of cells.

2.3.6 Most common cells used in cell migration experiments

Experiments of cell migration resort to some types of cells due to particular features that make them suitable for experimental manipulation and observation. Here, we introduce some of those cells, which will be computationally studied in the following sections.

The simplest mode of cell motion on flat surfaces is displayed by *keratocytes*. The keratocyte motile machinery consists of a 2D network of actin filaments. The network is subjected to myosin contraction at the cell's rear and forms a dense and quasi-stationary 2D structure at the cell's front called *lamellipodium*. The lamellipodium exerts protrusive forces on the cell's membrane. The actin network is connected to the substrate through adhesion clutches. This connection, mediated by integrin, permits the transmission of the actomyosin forces to the environment and, thus, the motion of the cell. Keratocytes possess many features that make them suitable for studying cell migration. For instance, they migrate spontaneously (they do not require any external stimulus) and their cellular motile machinery is simple and robust. In fact, Euteneuer and Schliwa observed that enucleated fragments of keratocytes exhibit the same motile machinery as the intact keratocytes [66], which allows direct experimental validation of simple cell migration models that do not consider the cell's nucleus.

Dictyostelium discoideum and *neutrophils* are the most common cells used to study amoeboid motion. Let us focus on *Dictyostelium*, which contrary to neutrophils, perform spontaneous migration. *Dictyostelium* is an elongated and highly deformable cell that achieves motion via rapidly protruding and retracting extensions generally called *pseudopods*. Pseudopods are dynamic actin-rich protrusions that locally drive the cell membrane outwards. Pseudopod growth is controlled by membrane signaling molecules such as, e.g., PIP3 [188]. Amoeboid motion results from the balance between myosin-induced contraction and alternating cycles of pseudopod extension. The *pseudopod-centered view* [92] states that external stimuli are not required for pseudopod formation. When subject to external chemical signals, the location of the growing pseudopods is biased by the extracellular chemical factors. Therefore, the *pseudopod-centered view* accounts for the spontaneous migration observed in *Dictyostelium*. The *pseudopod-centered view* is contrary to the *signal-centered view*, which states that external stimuli are necessary for pseudopod formation. The chemotactic response of *Dictyostelium* is triggered by the association between the membrane receptors and the extracellular factors. Receptor activation produces reactions that modify the dynamics of the membrane signaling molecules that control pseudopod growth.

Finally, collective migration is usually studied in the form of confluent epithelial monolayers. The wound-scratch assay [148,151] is the most common experimental approach to study collective motion. Madin-Darby canine kidney (MDCK) cells [191], normal rat kidney (NRK) cells [148], or keratocytes [153] are some examples of cells used in experiments of collective migration.

3 Mathematical models

We begin this section by presenting a general overview of the mathematical models that, in our opinion, settled the bases for modeling cell motility. Then, we introduce the phase-field method, i.e., a formulation employed to capture the moving cell. Finally, we review the state of the art of the phase-field models of individual and collective cell migration.

3.1 Overview

The literature related to modeling of cell migration is extensive. In this section, we will mention what we consider the most prominent models. Mathematical models of cell motility are based on experimental and theoretical evidence, which includes the study of cell-motion patterns [74,150, 175,201,202], modes of cell migration [72,105,177], cytosol dynamics [22,49,83,121,194], or the regulatory systems involved in the membrane signaling pathways [63,111,

119,158]. Computational modeling has been recently proposed as an effective way to test conceptual models of cell motility. Detailed reviews of cell migration models may be found in [36,57,87,131,177,207]. There may be multiple classifications of the computational models of cell motility, which vary according to the factors selected to carry out the sorting. Here, we propose three classification criteria:

Scale. The models may be classified according to their scale in: (1) Subcellular models, which explain particular processes occurring at some regions of the cell, such as actin polymerization [15,43,101], bleb formation [173], actomyosin network dynamics [28,100], or cell-substrate adhesion [46, 63]; (2) Cellular-scale models that simulate the entire cell and may focus either on the membrane molecule dynamics [109,129], on the laws governing the cytosolic components [7,16,165], or couple both compartments [126,137]; (3) Tissue-level models representing collective motion [8, 124,155,203] (more information in the last paragraph of this section).

Cell deformation. Some models assume that the geometry of the cell stays fixed during motion [102,174], while others consider cell deformation [114,118,143].

Cell shape formulation. The models that consider cell shape as an unknown can be classified by the formulation used to determine the cell morphology. We highlight three different alternatives: (1) Interface-tracking approach, where the boundary, i.e., the cell's membrane, is explicitly tracked (e.g., through Lagrangian marker points [85,192], the immersed boundary method [45,172], or moving bulk and surface meshes [62,118]); (2) Level set method, which uses a time-evolving distance function, defined on a fixed domain, to locate the cell membrane [141,167]; (3) Phase-field method, which, as the level set method, avoids the use of moving meshes. The phase-field method resorts to an auxiliary field to identify the region occupied by the cell [24,60, 135] (more details in Sect. 3.2).

The complexity of cellular-scale models has increased over the years (from 1D [82] to 3D [182] models and from cells with fixed geometry [19] to highly deformable cells [137]). Most cellular-scale models have focused on the rheology of the actin network. Earlier models treated the network as a viscoelastic gel represented by a set of nodes connected by viscoelastic springs [31]. The assumption of continuum mechanics to model the viscoelastic gel [81,106] leads to the concept of active stress [44,95], which allows to account for protrusion and contraction. Thus, the actomyosin network has been modeled as a Newtonian [18,19] or non-Newtonian [159], compressible [165] or incompressible [24] fluid. The momentum conservation equation includes the forces caused by the cell motion machinery and may be coupled to myosin, actin, and adhesion complex dynamics [19,165]. A more detailed theory considers the cytosol as a multiphase fluid [11,52,104,172], where one phase represents the cytosolic fluid and the other the actin network. According to [131], the most accurate description of the cytosol corresponds to a poroviscoelastic material. A different approach to model the actin network dynamics resorts to a polarization vector, which accounts for the polar orientation of the filaments [60,115,208] (more details in Sect. 3.3).

Cell motility is controlled by a group of molecules that activate the cytosolic motile machinery. A number of mathematical models have studied the interactions of these molecules along the signaling pathway, which mainly occur in the vicinity of the membrane. Some models have successfully reproduced the overall behavior of these molecules by using a set of activators and inhibitors located in the membrane (e.g., Meinhardt's model [129] and local-excitation global-inhibition (LEGI) [109] models). Those models may be extended by adding other modules that account for cell polarization, cytoskeleton dynamics, or biased excitable networks (BEN) [59,90,91]. Other models have studied in detail the interactions between the signaling molecules (e.g., the Rho GTPases and PIs families) [75,123,174]. A different approach resorted to a phenomenological abstraction of the signaling events, such as, e.g., the wave-pinning model [134,145] or stochastic models [30,187]. To gain further insight into these signaling models, many authors have solved them on deformable geometries [62,141,167]. For instance, in [141], the velocity of the cell membrane is assumed to be proportional to the activator concentration and this leads to a criteria that permits to update the cell's shape.

A number of models have studied the interaction between the cell and its environment [41,86,99,156,183]. For instance, [156] proposed a 3D model of mesenchymal motion that couples the dynamics of the membrane signaling molecules with the extension of filopodia in the ECM. In [156], the ECM is assumed to be an elastic body, while in other works (e.g., [86]) the ECM is modeled as a viscoelastic solid. The authors of [183] proposed a hybrid model to study amoeboid migration in confined matrix environments. In [183], the nucleus, the actin cortex, the cell membrane, and the ECM fibers are represented by sets of discrete nodes.

The migration of multicellular systems (see Fig. 6) has been and continues to be modeled by using continuum approaches [186,193], in which mass and momentum balance equations account for the tissue dynamics. A paradigm of a continuum model for multicellular chemotaxis is [97], which includes cellular and chemoattractant density fields. Cell dynamics in [97] is modeled as a Brownian motion, an approach widely used in multicellular systems [14,74,157]. Collective migration models have also resorted to the so-called agent-based models. In agent-based models, the location of each cell is explicitly tracked, which permits a more direct modeling of cellular processes such as cell proliferation, cell death, cell-cell adhesion, or cell migration. Agent-

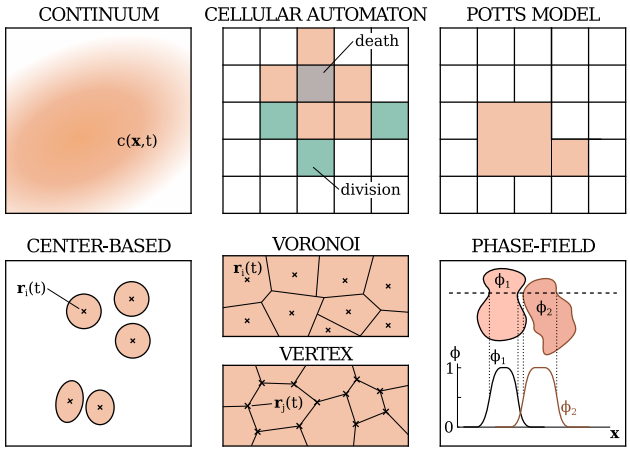

Fig. 6 Tissue-level models. Schematic representation of different types of multicellular models.

based models permit to account for cellular-level inhomogeneities. Inspired by [36, 189], we classify agent-based models as lattice or off-lattice models. Lattice models employ a fixed geometrical lattice; see Fig. 6. The cellular automaton [84, 108, 122, 140] is an example of lattice model where each cell occupies one lattice site. In the cellular automaton approach, cells may be in different states and a set of rules controls the transition between states. The cellular Potts model [27, 123, 163] constitutes an example of lattice model with a cell spanning several sites. In this case, a Hamiltonian energy determines the shift between the different cellular states. Off-lattice models do not restrict the location of the cell to a specific spatial discretization. Off-lattice models are divided in center-based and deformable-cell models. Center-based models establish force balance equations (or energy functionals) as a function of the position of the cells centers ($\mathbf{r}_i$ in Fig. 6). Center-based models may assume a fixed (or slightly deformable) cell geometry [1, 40, 61, 147, 190, 209] or a cellular shape obtained from the Voronoi diagram of the cells centers [23, 88, 128]. Voronoi models permit a more accurate modeling of the cell geometry and the cell-cell interactions in case of confluent layers. Deformable-cell models formulate the evolution equations based on the set of nodes ($\mathbf{r}_j$ in Fig. 6) that define the geometry of the cells. Voronoi and deformable-cell models allow to represent arbitrary cell shapes. Vertex models [67, 68, 113], a prime example of deformable-cell models, track the dynamics of the polygon vertexes that delimit the cell. According to the previous classification, multicellular phase-field models [116, 142, 146] are considered deformable-cell models. A detailed description of phase-field models for collective migration may be found in Sect. 3.4. Finally, hybrid models couple agent-based and continuum models to overcome the specific limitations of each model alone. Hybrid models have simulated processes such as, e.g., angiogenesis [70], durotaxis [65], or wound healing [80, 204].

3.2 The phase-field method

Cell migration can be thought of as a moving boundary problem (MBP), where the boundary represents the cell membrane. The numerical treatment of MBP is quite complex. The phase-field method [12, 48, 64, 77, 79, 152] (also known as diffuse-interface or diffuse domain method) has emerged as a mathematical theory that reformulates the MBP as partial-differential equations (PDEs) posed on a known and fixed computational domain. This methodology introduces a new variable, the phase field ϕ, defined on the entire domain, which serves as a marker of the location of the cell ($\phi = 1$ inside the cell and $\phi = 0$ outside). The interface, i.e., the cell membrane, displays a rapid but smooth transition of ϕ; see Fig. 7. The interface width is controlled by the regularization parameter ε. In many cases, one may prove that the phase-field problem converges to its associated MBP as ε tends to zero. This is why the MBP is also called sharp-interface model in the phase-field community. However, phase-field problems do not necessarily possess an associated sharp-interface problem. The evolution equations of the phase-field problem can be derived directly from an energy functional that controls the dynamics of the phases by using the classical theory of thermodynamics and Coleman-Noll-type approaches [53, 185]. For example, in case of the canonical Allen-Cahn (AC) [6] and Cahn-Hilliard (CH) [35] equations, the energy functional may be written as

$$\mathscr{F}^{\varepsilon}[\phi] = \int_{\Omega} \Psi \mathrm{d}\Omega = \int_{\Omega} \left(\frac{G(\phi)}{\varepsilon} + \frac{\varepsilon}{2} |\nabla \phi|^2 \right) \mathrm{d}\Omega, \tag{1}$$

where the function $G(\phi)$ is a double-well potential with minima in $\phi = 0$ and $\phi = 1$. The functional derivative of $\mathscr{F}^{\varepsilon}$, called chemical potential, takes the expression

$$\frac{\delta \mathscr{F}^{\varepsilon}}{\delta \phi} = \frac{G'(\phi)}{\varepsilon} - \varepsilon \nabla^2 \phi. \tag{2}$$

By establishing constitutive relations and imposing energy dissipation of the system, we can derive the AC and CH equations (see [79] for more details), which may be written, respectively, as

$$\frac{\partial \phi}{\partial t} = -m(\phi) \frac{\delta \mathscr{F}^{\varepsilon}}{\delta \phi}, \qquad \frac{\partial \phi}{\partial t} = \nabla \cdot \left[m(\phi) \nabla \frac{\delta \mathscr{F}^{\varepsilon}}{\delta \phi} \right], \tag{3}$$

where $m(\phi)$ is a positive function. The AC equation assumes non-conserved mass dynamics, while CH assumes mass conservation. A different approach to derive a diffuse-interface problem consists of diffusifying the corresponding sharp-interface problem; see [79] for more details.

Although the use of the phase-field method avoids the numerical issues associated to moving boundaries, new computational challenges emerge: (i) Regions of large gradients of ϕ in the neighborhood of the interface. The use of local refinement methods [117,195] is appropriate; (ii) Phase-field theories are usually governed by higher-order PDEs, which cannot be directly solved with classical finite element methods (FEM). Isogeometric analysis [89] is a novel computational method that allows straightforward discretization of higher-order PDEs on mapped geometries (see [78]); (iii) The dynamics of the phase field, which may include the emergence and vanishing of interfaces, involves multiple time scales.

We believe the phase-field approach is an ideal methodology for cell migration models because it can accomplish three important goals simultaneously:

Define cell shape. As mentioned above, the phase field $\phi(\mathbf{x},t)$ identifies the region occupied by the cell. If we make the assumption that cell membrane deformations are driven by the F-actin network, our goal is to move the interface with a velocity $\mathbf{u}(\mathbf{x},t)$, where $\mathbf{u}$ is the velocity of the actin network. At this point, let us assume, for simplicity, that $\mathbf{u}$ is known. Biben and collaborators [24,25] proposed a phase-field approach for vesicle dynamics in which the interface moves with velocity $\mathbf{u}$ while ϕ maintains a hyperbolic tangent profile. The phase-field equation proposed in [24], which can be interpreted as a perturbation of the level set equation $\frac{\partial\phi}{\partial t}+\mathbf{u}\cdot\nabla\phi=0$, is written as

$$\frac{\partial\phi}{\partial t}+\mathbf{u}\cdot\nabla\phi=\Gamma_\phi\left(\varepsilon\nabla^2\phi-\frac{G'(\phi)}{\varepsilon}+c\varepsilon|\nabla\phi|\right), \tag{4}$$

where Γ_ϕ is a constant and $c=-\nabla\cdot(\nabla\phi/|\nabla\phi|)$ is the curvature of the interface. Contrary to the level set equation, in which ϕ takes the form of a distance function, Eq. (4) [in particular, the right-hand side of Eq. (4)] imposes a hyperbolic tangent profile for ϕ. Note that Eq. (4) allows for cell volume changes. Cell volume conservation should be imposed through the dynamics of the velocity $\mathbf{u}$. Another possibility is to include a volume-conservation term in Eq. (4); see, e.g., [166,196].

Localize evolution equations to moving volumes and surfaces. The phase-field method allows us to compute the dynamics of compounds located in moving domains by using a fixed mesh. Examples of these compounds are the cytoskeleton constituents living inside the cell, extracellular chemoattractants, or proteins that move throughout the membrane. Based on [112,178], we show how evolution equations posed on moving domains can be reformulated on a bigger and fixed domain. Let us consider a generic compound with density $\rho(\mathbf{x},t)$, which is located in the moving domain $\Omega_\rho(t)$. Let us assume that $\Omega_\rho(t)$ represents the cell's interior; see Fig. 7. The evolution equations for ρ are written as

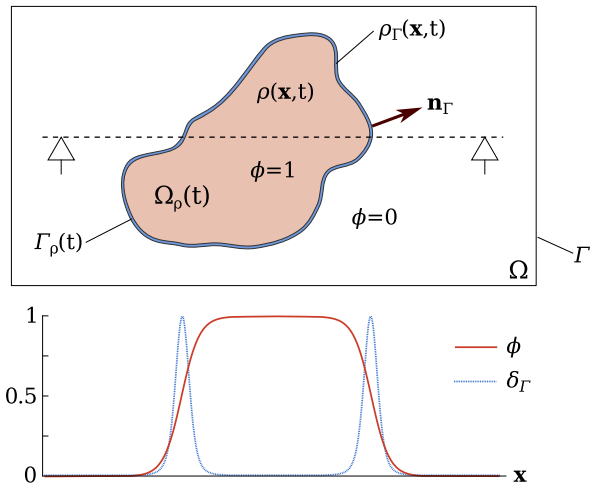

Fig. 7 Phase-field approach for the motile cell problem. The cell is represented by the moving domain $\Omega_\rho(t)$, while the membrane is $\Gamma_\rho(t)=\partial\Omega_\rho(t)$. We consider a cytosolic compound ρ and a membrane compound ρ_Γ. The phase-field problem is posed on the fixed domain Ω. On the bottom, profiles of the phase field ϕ and the membrane marker δ_Γ.

$$\frac{\partial\rho}{\partial t}+\nabla\cdot(\rho\mathbf{u}_\rho)=\nabla\cdot(D_\rho\nabla\rho)+r_\rho \qquad \text{in } \Omega_\rho(t), \tag{5}$$

$$D_\rho\nabla\rho\cdot\mathbf{n}_\Gamma+\rho(\mathbf{u}_\Gamma\cdot\mathbf{n}_\Gamma-\mathbf{u}_\rho\cdot\mathbf{n}_\Gamma)=-j \qquad \text{on } \Gamma_\rho(t), \tag{6}$$

where we consider diffusion (D_ρ), a reactive term r_ρ, and a bulk velocity $\mathbf{u}_\rho(\mathbf{x},t)$. The boundary condition in Eq. (6) is posed on the cell membrane $\Gamma_\rho(t)=\partial\Omega_\rho(t)$ and includes a prescribed flux j across the membrane. The unit normal to $\Gamma_\rho(t)$ is denoted as $\mathbf{n}_\Gamma$. The velocity of $\Gamma_\rho(t)$ is denoted as $\mathbf{u}_\Gamma(\mathbf{x},t)$, which does not necessarily coincide with $\mathbf{u}_\rho$. Let us also consider a membrane-bound compound $\rho_\Gamma(\mathbf{x},t)$ whose evolution equation is written as

$$\frac{\partial\rho_\Gamma}{\partial t}+\nabla_\Gamma\cdot(\rho_\Gamma\mathbf{u}_\Gamma)=\nabla_\Gamma\cdot(D_\Gamma\nabla_\Gamma\rho_\Gamma)+r_\Gamma+j \quad \text{in } \Gamma_\rho(t), \tag{7}$$

where D_Γ is the diffusion coefficient, r_Γ is a generic reactive term, and j is the mass flux term that couples the compounds ρ and ρ_Γ. The operator ∇_Γ denotes ∇ on the surface Γ_ρ. Eqs. (5)–(7) constitute the so-called sharp-interface problem. Let us consider now a larger and fixed domain Ω such that $\Omega_\rho(t)\subset\Omega$ for all t. Let us also assume that we know the functions ϕ and δ_Γ, which define the spatial location of the cell and the membrane, respectively; see Fig. 7. The phase field ϕ can be governed by Eq. (4) with $\mathbf{u}=\mathbf{u}_\Gamma$, while δ_Γ may be defined in terms of ϕ such that, e.g., $\delta_\Gamma(\phi)=\varepsilon|\nabla\phi|^2$ or $\delta_\Gamma(\phi)=2G(\phi)/\varepsilon$. The equivalent diffuse-interface prob-

lem, posed in Ω, can be stated as

$$\frac{\partial(\phi\rho)}{\partial t}+\nabla\cdot(\phi\rho\mathbf{u}_\rho)=\nabla\cdot(D_\rho\phi\nabla\rho)+\phi r_\rho-\delta_\Gamma j \ \text{ in } \Omega, \tag{8}$$

$$\frac{\partial(\delta_\Gamma\rho_\Gamma)}{\partial t}+\nabla\cdot(\delta_\Gamma\rho_\Gamma\mathbf{u}_\Gamma)=\nabla\cdot(D_\Gamma\delta_\Gamma\nabla\rho_\Gamma)+\delta_\Gamma r_\Gamma+\delta_\Gamma j \quad \text{in } \Omega, \tag{9}$$

where the functions ρ and ρ_Γ are now defined in Ω, such that ρ_Γ is extended off Γ_ρ constant in the normal direction. Eqs. (8)–(9) constitute the diffuse-interface problem, which is equivalent to the sharp-interface problem as the regularization parameter ε tends to zero [112,178]. The dynamics of an extracellular compound can be controlled by an equation analogous to Eq. (8), substituting the cellular marker ϕ by a marker of the extracellular environment (e.g., $1-\phi$).

Control cellular dynamics through an energy functional. The phase-field equation that controls cell dynamics can be sometimes derived from an energy functional. In that case, the derivation of the phase-field equation is based on free-energy-dissipation principles [see, e.g., Eqs. (1)–(3)], which leads to problems with a notion of nonlinear stability. The energy functional may account for different cellular phenomena such as, e.g., the membrane surface tension, cell volume conservation, or chemotaxis. This approach, in which cell dynamics is controlled by an energy functional, is also valid for multicellular systems. In fact, the phase-field formulation permits a simple treatment of intercellular interactions such as cell-cell adhesion or cell-cell repulsion. A more detailed description of the cellular dynamics requires the coupling of the phase field with other unknowns that account for the dynamics of different elements such as, e.g., F-actin, myosin, or adhesion complexes. The problem becomes computationally more intensive as the number of unknowns increases. Thus, it is important to include in the model only the elements that are essential to address the question we are interested on, especially in the case of multicellular systems.

Let us focus on the general case of a multicellular system comprised of N cells. Each cell n is represented by a single unknown, the phase field $\phi_n(\mathbf{x},t)$. The functional of the multicellular system is written as $\mathscr{F}[\phi_1,\cdots,\phi_N]=\sum_n\mathscr{F}_n[\phi_n]$, where $\mathscr{F}_n$ is the functional of each cell (some examples of $\mathscr{F}_n$ may be found in Sect. 3.4). Given the functional $\mathscr{F}$, the evolution equation for each cell is written as

$$\frac{\partial\phi_n}{\partial t}+\mathbf{u}_n\cdot\nabla\phi_n=j_n, \tag{10}$$

where $\mathbf{u}_n$ and j_n are expressed in terms of the chemical potential[4] as

$$j_n=-\Gamma_n\frac{\delta\mathscr{F}}{\delta\phi_n}, \qquad \mathbf{u}_n=\xi_n^{-1}\int_\Omega\frac{\delta\mathscr{F}}{\delta\phi_n}\nabla\phi_n\,\mathrm{d}\Omega. \tag{11}$$

In Eq. (11), Γ_n and ξ_n are constants that control the time scale of the problem. One may prove that for velocity fields that are uniform in space, $\mathscr{F}$ decreases with time along solutions to Eqs. (10)–(11). The motion of each cell can be modeled through an appropriate term in the functional $\mathscr{F}_n$ (e.g., [142,170] resort to this approach to model chemotaxis) or by adding an active velocity to the term $\mathbf{u}_n$ (more details in Sect. 3.4). Eq. (10) can be coupled with other PDEs to account for processes not modeled through the functional $\mathscr{F}$.

3.3 Individual cell migration

From our point of view, there are two approaches that successfully reproduce cell motility. The first approach introduces the polarization vector $\mathbf{p}$, which represents the average orientation of the actin filaments. This approach assumes that filaments normal to the membrane cause protrusion, i.e., that $\mathbf{p}$ controls the advection of the phase field. The second approach focuses on the rheology of the actin network, treated as a fluid with velocity $\mathbf{u}$. In that case, the motion of the cell is controlled by Eq. (4). In the two approaches, the phase-field equation is coupled to a set of equations that account for the biomechanical processes and constituents considered in the problem (more details below). Although the two approaches can be explained from a biomechanical point of view, they display several conceptual differences that we describe in the following paragraphs.

Ziebert and collaborators [208] proposed a phase-field model that includes the polarization $\mathbf{p}$ of actin filaments. The model was subsequently expanded in [115,206], where the phase field $\phi_p(\mathbf{x},t)$ and $\mathbf{p}(\mathbf{x},t)$ were coupled to the active adhesion complex density $\mathsf{A}(\mathbf{x},t)$ and the in-plane deformation of the substrate $\mathbf{d}(\mathbf{x},t)$. The model describes 2D keratocyte migration, and together with [165,166], constitute the first phase-field models to simulate realistic keratocyte morphodynamics; see Fig. 8. Instead of using Eq. (4), the phase field in [115,206,208] is controlled by the equation

$$\frac{\partial\phi_p}{\partial t}+\alpha\mathsf{A}\mathbf{p}\cdot\nabla\phi_p=D_\phi\nabla^2\phi_p-\phi_p(1-\phi_p)(\delta_p[\phi_p,\mathbf{p}]-\phi_p), \tag{12}$$

where $\delta_p[\phi_p,\mathbf{p}]=\frac{1}{2}+\mu_p(\int_\Omega\phi_p\,\mathrm{d}\Omega-A_0)-\sigma|\mathbf{p}|^2$. The phase field ϕ_p is advected by $\alpha\mathsf{A}\mathbf{p}$, where α is a constant. Thus, there is a contribution to the membrane velocity that is proportional to $\mathbf{p}$ and A. Note that Eq. (12) is a modified AC

[4] The derivation of j_n and $\mathbf{u}_n$ is based on constitutive relations and energy dissipation's principles; see [146,200] for more details.

equation. In fact, the right-hand side of Eq. (12) is equivalent to the right-hand side of the AC equation if $\delta_p = 1/2$. Values of δ_p larger (smaller) than $1/2$ lead to the shrinkage (expansion) of the cell. Eq. (12) also accounts for cell volume conservation through the μ_p-term in the function δ_p and myosin-induced contraction through the σ-term in δ_p (more details in [208]). The dynamics of $\mathbf{p}$ is governed by the equation

$$\frac{\partial \mathbf{p}}{\partial t} = D_p \nabla^2 \mathbf{p} - \beta_p \nabla \phi_p - \frac{\mathbf{p}}{\tau_1} - \frac{(1-\phi_p^2)\mathbf{p}}{\tau_2} - \gamma(\nabla \phi_p \cdot \mathbf{p})\mathbf{p}. \tag{13}$$

Note that the equation for $\mathbf{p}$ is not localized to the cell by using the phase-field method, as done in Eq. (8). Instead, the τ_2-term drives $\mathbf{p}$ to zero outside the cell. Eq. (13) considers the diffusion (D_p) of $\mathbf{p}$, actin polymerization normal to the membrane (β_p-term), actin depolymerization at constant rate (τ_1-term), and a symmetry breaking term to favor cell polarization (γ-term). The equation for adhesive bond dynamics is expressed as

$$\frac{\partial \mathsf{A}}{\partial t} = D_{\mathsf{A}} \nabla^2 \mathsf{A} + \phi_p (a_0 |\mathbf{p}|^2 + a_{nl} \mathsf{A}^2) - \left[d(|\mathbf{d}|) + s\mathsf{A}^2 \right] \mathsf{A}, \tag{14}$$

which considers diffusion (D_{A}), adhesive bonds formation (a_0) and reinforcement (a_{nl}), detachment of adhesions as a function of the substrate displacements $\mathbf{d}$ (according to the function d), and adhesion bond saturation depending on the parameter s. As in Eq. (13), adhesion dynamics is weakly localized to the cell, in this case by restricting adhesion formation and reinforcement to the cell's interior through the marker ϕ_p. Eq. (14) is coupled to the substrate displacement $\mathbf{d}$, in such a way that adhesion detachment rate increases as $\mathbf{d}$ increases [206]. The model considers the substrate as an incompressible viscoelastic solid that undergoes overdamped motion. The in-plane displacement of the horizontal substrate is dictated by the equation [115]

$$\eta \frac{\partial \mathbf{d}}{\partial t} = -(G\mathbf{d} - \mathbf{T}), \tag{15}$$

where η is an effective viscous friction coefficient and G an effective spring constant. $\mathbf{T}(\mathbf{x},t)$ is the stress exerted by the cell on the substrate. Assuming that the forces applied by the cell match a viscous drag force (i.e., $\mathbf{T} - \varsigma \mathbf{u} = 0$ where ς is a friction coefficient) and that the velocity $\mathbf{u}(\mathbf{x},t)$ is expressed as a function of $\mathsf{A}\mathbf{p}$, the stress may take the form $\mathbf{T} = -\phi_p \varsigma \mathsf{A}(\mathbf{p} - \int_\Omega \phi_p \mathsf{A}\mathbf{p}\, \mathrm{d}\Omega / \int_\Omega \phi_p \mathsf{A}\, \mathrm{d}\Omega)$ [115]. Eqs. (12)–(15) display slight differences throughout the different works published [115,206,208]. The model for 2D keratocyte migration defined by Eqs. (12)–(15) has been used to simulate steady motion (see Fig. 8B), oscillatory, bipedal, and stick-slip motion (see Fig. 8A), durotaxis, and migration in micropatterned substrates. Many authors leveraged this model

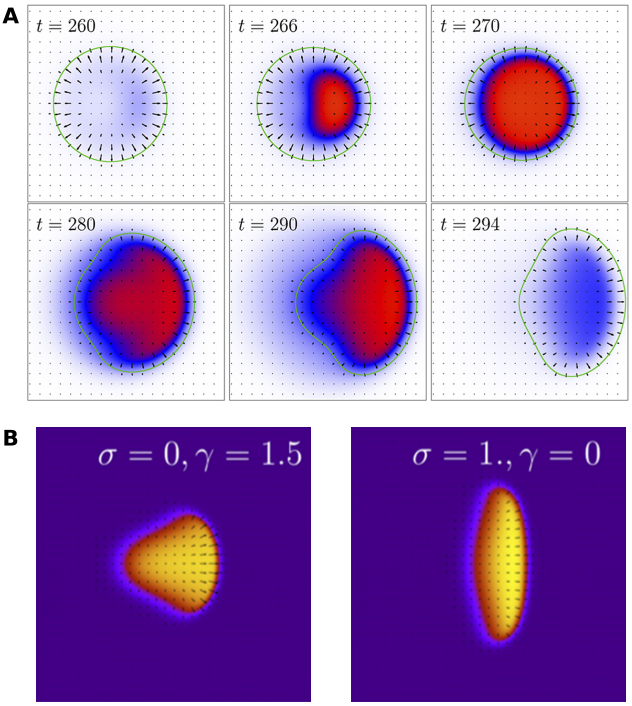

Fig. 8 2D keratocyte migration corresponding to the simulation results of [206]. **A** Time evolution of stick-slip motion. The green line identifies the cell membrane, the arrows represent the polarization ($\mathbf{p}$) distribution, and the color scale accounts for the adhesion (A) distribution. **B** Stationary state of motile keratocytes for different values of the parameters σ and γ; see Eqs. (12) and (13). Reproduced from [206].

to further study cell migration [60,125,130,133,154,181,182,198,199]. For instance, [181] proposed a phase-field model for active droplet motion. The model is derived from an energy functional that depends on ϕ_p and $\mathbf{p}$. The model also includes the velocity of an incompressible fluid located inside and outside the droplet. The model was expanded to 3D to successfully simulate 3D cell crawling on surfaces [182]. A similar approach was employed in [125] to reproduce migration driven by active polar gels. The phase-field model proposed in [60] accounts for the dynamics of pro-nucleation factors (PNF) inside the cell, which control actin polymerization (i.e., $\mathbf{p}$ dynamics) and consequently, cell motion. In [60], the PNF dynamics is not restricted to the cell's interior through the phase-field methodology. Instead, a vanishing PNF density is numerically imposed outside the cell. The model reproduces actin-polymerization waves and amoeboid motion of 2D cells. The approach developed by Ziebert and collaborators produced excellent results and proposed a novel description for actin networks, adhesive bounds dynamics, and the coupling to a viscoelastic substrate. Further extensions and refinements of this family of models could focus on: i) an explicit description of cytoskeletal flow and stresses; ii) a formulation in which the localization of the cytosolic compounds to the cell's interior is imposed more

strongly, e.g., using the approach illustrated in Eqs. (5)–(9); iii) a more direct consideration of contraction and protrusion forces in the cell's interior.

The second approach to model individual cell migration resorts to a velocity field $\mathbf{u}$, rather than the polarization $\mathbf{p}$, to drive membrane displacements. Inspired by [24,159] and their own previous work [166], Shao and collaborators proposed a 2D phase-field model [165] for keratocyte morphodynamics. The model proposed a force-balance equation for the actin network dynamics, which accounts for the membrane surface tension and bending resistance, actin protrusion, myosin contraction, adhesion to the substrate, and the viscosity of the network . The force-balance equation was coupled to F-actin, G-actin, and myosin dynamics, which are localized to the cell by means of the phase-field method. The significance of this approach resides in the treatment of the actomyosin network as a viscous fluid [19,159] subjected to the forces exerted by the motile machinery. In addition to reproducing the steady state of moving keratocytes, the model was able to capture the experimentally-observed distribution of the actin network flow (including actin retrograde flow). The authors expanded the model to simulate oscillatory, bipedal, rotational motion, and turning cells [37,38,39]. The model proposed in [165] settled the bases for subsequent works that reproduced, e.g., spontaneous division and motility of active nematic droplets [76], amoeboid motion [126,135], migration in 3D fibrous environments [136], chemotaxis [137], or cell-substrate adhesion in channels [42]. In particular, we proposed a phase-field model of 3D amoeboid chemotactic migration [137], which also accounts for the interaction between the cell and rigid fibers (or obstacles). The model in [137] considers three time-evolving spatial domains: the cell, the membrane, and the extracellular environment; see Fig. 9A. The cell shape is defined by the phase field $\phi(\mathbf{x},t)$, which is advected by the velocity of the actin network $\mathbf{u}(\mathbf{x},t)$. We use Eq. (4) to control the dynamics of ϕ. We define the membrane marker in terms of ϕ as $\delta_m(\phi) = \exp\left[-\psi(\phi-1/2)^2\right]$, where ψ is a parameter controlling the thickness of the marker. Finally, the extracellular environment location is defined with the marker

$$\varphi(\phi, d_o(\mathbf{x})) = (1-\phi) f_\varphi(d_o(\mathbf{x})), \tag{16}$$

where the function f_φ takes the value 0 in the region occupied by the obstacles and 1 elsewhere ($d_o(\mathbf{x})$ denotes the distance to the obstacles; more details in [137]). From Eq. (16), it follows that $\varphi = 1$ outside the cell and the obstacles, and $\varphi = 0$ elsewhere; see Fig. 9A. We consider three cytosolic compounds: myosin, G-actin, and F-actin, with densities $\rho_m(\mathbf{x},t)$, $\rho_g(\mathbf{x},t)$, and $\rho_f(\mathbf{x},t)$, respectively. The actin network is treated as a Newtonian fluid with velocity $\mathbf{u}(\mathbf{x},t)$. We also consider a membrane-bound activator $a(\mathbf{x},t)$ that promotes actin nucleation and an extracellular chemoattractant $q(\mathbf{x},t)$ that biases the activator dynamics. Myosin dynamics is restricted to the cell's interior and is governed by the convection-diffusion equation

$$\frac{\partial(\phi\rho_m)}{\partial t} + \nabla\cdot(\phi\rho_m\mathbf{u}) - \nabla\cdot\left[D_m(\rho_f)\phi\nabla\rho_m\right] = 0, \tag{17}$$

where myosin diffusion depends on the F-actin density according to the function $D_m(\rho_f)$; see [137]. Phase transformations between G-actin and F-actin (i.e., actin polymerization and depolymerization) are described by the functional

$$\begin{aligned}\mathscr{F}_\rho[\rho_f,\rho_g] = \int_\Omega \phi\left[\frac{\varepsilon_f^2}{2}|\nabla\rho_f|^2 + \frac{\varepsilon_g^2}{2}|\nabla\rho_g|^2 + F_\rho\left(\rho_f,\rho_g,a\right)\right]\mathrm{d}\Omega \\ + \lambda_N\left(N_{A0} - N_A[\rho_f,\rho_g]\right),\end{aligned} \tag{18}$$

where ε_f and ε_g are constant parameters, $N_A[\rho_f,\rho_g] = \int_\Omega \phi(\rho_f+\rho_g)\mathrm{d}\Omega$ is the amount of actin inside the cell, N_{A0} denotes N_A at the initial time, λ_N is a Lagrange multiplier to keep N_A constant in time, and F_ρ is the function that controls the actin phase transitions depending on the activator a, expressed as

$$\begin{aligned}F_\rho\left(\rho_f,\rho_g,a\right) = 10\left(\rho_f-\rho_f^{\mathrm{pr}}\right)^2\left(\rho_f-\rho_f^{\mathrm{pa}}\right)^2 + 7.5\left(\rho_g-\rho_g^{\mathrm{eq}}\right)^2 \\ + I(a)(\rho_f-\rho_f^{\mathrm{pr}})^2\left[\rho_f + \kappa(a)I(a)\right].\end{aligned} \tag{19}$$

More details on this formulation may be found in [137]. According to Eq. (19), G-actin displays only one stable density ρ_g^{eq} (local minimum of F_ρ), while F-actin exhibits two stable densities, ρ_f^{pr} and ρ_f^{pa}, which represent protrusive (e.g., lamellipodium or pseudopod) and non-protrusive (passive) actin structures, respectively. High values of a promote protrusive structures (see Fig. 9B bottom), while low values of a favor the presence of passive networks (see Fig. 9B top). The approach proposed here constitutes an expansion of the wave-pinning model [134], where we incorporate the effect of a nucleating agent a that promotes actin polymerization. In fact, if we neglect the influence of a (i.e., if we take $I(a)=0$), our model for actin phase transformations is analogous to the wave-pinning model [134]. The governing equations for F-actin and G-actin dynamics are written as

$$\begin{aligned}\frac{\partial(\phi\rho_f)}{\partial t} + \nabla\cdot(\phi\rho_f\mathbf{u}) &= -\Gamma_f\frac{\delta\mathscr{F}_\rho}{\delta\rho_f} \\ &= \Gamma_f\left[\varepsilon_f^2\nabla\cdot(\phi\nabla\rho_f) - \phi\frac{\partial F_\rho}{\partial\rho_f} + \lambda_N\phi\right],\end{aligned} \tag{20}$$

$$\begin{aligned}\frac{\partial(\phi\rho_g)}{\partial t} + \nabla\cdot(\phi\rho_g\mathbf{u}) &= -\Gamma_g\frac{\delta\mathscr{F}_\rho}{\delta\rho_g} \\ &= \Gamma_g\left[\varepsilon_g^2\nabla\cdot(\phi\nabla\rho_g) - \phi\frac{\partial F_\rho}{\partial\rho_g} + \lambda_N\phi\right],\end{aligned} \tag{21}$$

where Γ_f and Γ_g are constants. Note that Eqs. (17), (20), and (21) employ the marker ϕ to localize the ρ_m, ρ_f, and ρ_g dynamics to the cytosol; see Eq. (8). If we assume appropriate boundary conditions and strong actin conservation

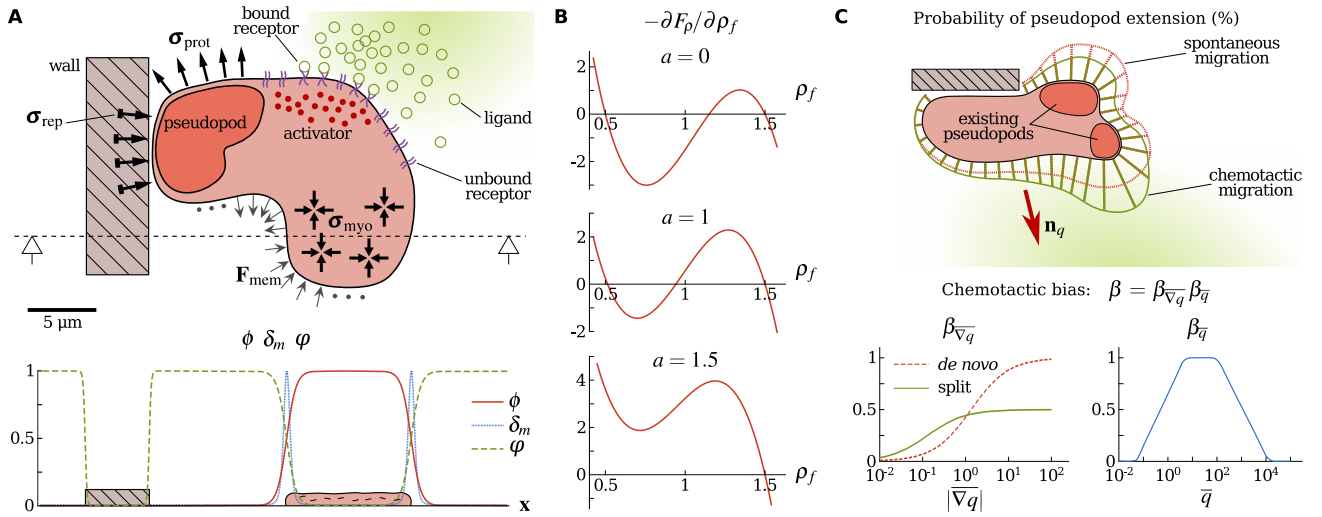

Fig. 9 Phase-field model of amoeboid chemotactic motion. **A** Cell forces and membrane-signaling reactions. On the bottom, phase-field approach employed to define the location of the cell (ϕ), the membrane (δ_m), and the extracellular environment (φ). **B** Dependence of the actin free-energy functional $\mathscr{F}_\rho$ on the activator a. The plots correspond to $\rho_f^{\text{pa}} = 0.5$ and $\rho_f^{\text{pr}} = 1.5$. **C** On the top, probability distribution of pseudopod extension. The probability distribution corresponding to spontaneous migration (red) is biased according to β and $\mathbf{n}_q$ to account for chemotactic migration (green). β is the chemotactic bias, while $\mathbf{n}_q$ indicates the chemotactic gradient direction. On the bottom, chemotactic bias (β) produced by the characteristic gradient ($\overline{\nabla q}$) and the average level ($\overline{q}$) of chemoattractant along the membrane, derived from [73, 171, 187]. The value $\beta_{\overline{\nabla q}}$ depends on the type of pseudopod (*de novo* or split). More details in [137].

(i.e., $\partial N_A/\partial t = 0$), from the evolution equations of ρ_f and ρ_g (Eqs. (20) and (21), respectively) and the definition of $N_A[\rho_f, \rho_g]$, we can obtain the value of the Lagrange multiplier

$$\lambda_N = \frac{\Gamma_f \int_\Omega \phi \frac{\partial F_\rho}{\partial \rho_f} \mathrm{d}\Omega + \Gamma_g \int_\Omega \phi \frac{\partial F_\rho}{\partial \rho_g} \mathrm{d}\Omega}{(\Gamma_f + \Gamma_g) \int_\Omega \phi \mathrm{d}\Omega}. \tag{22}$$

In addition, we can reformulate the evolution equation for G-actin by assuming that $N_A = N_{A0}\ \forall t$ and that diffusion dominates the ρ_g dynamics, i.e., $\rho_g(\mathbf{x}, t) \to \rho_g(t)$. From the definition of $N_A[\rho_f, \rho_g]$ we obtain

$$\rho_g(t) = \frac{N_{A0} - \int_\Omega \phi \rho_f \mathrm{d}\Omega}{\int_\Omega \phi \mathrm{d}\Omega}. \tag{23}$$

The actin network flow $\mathbf{u}$ is governed by the force balance equation

$$\nabla \cdot \left(\boldsymbol{\sigma} + \boldsymbol{\sigma}_{\text{myo}} + \boldsymbol{\sigma}_{\text{prot}} + \boldsymbol{\sigma}_{\text{rep}}\right) + \mathbf{F}_{\text{mem}} + \mathbf{F}_{\text{adh}} = 0, \tag{24}$$

which accounts for the forces caused by the motile machinery; see Fig. 9A. In Eq. (24) we consider the viscous stress of the actin network $\boldsymbol{\sigma} = \phi[\mu(\nabla \mathbf{u} + \nabla \mathbf{u}^T) + \lambda(\nabla \cdot \mathbf{u})\mathbf{I})]$, where μ and λ are the viscosity coefficients and $\mathbf{I}$ is the identity tensor. We also consider the isotropic myosin-driven contraction of the network $\boldsymbol{\sigma}_{\text{myo}} = \phi \rho_m \eta_m(\rho_m)\mathbf{I}$ and the protrusive stress $\boldsymbol{\sigma}_{\text{prot}} = -\phi \rho_f \eta_f(\rho_f)\delta_f \nabla\phi \otimes \nabla\phi$ exerted by the pseudopods on the membrane. The terms η_m and η_f determine the strength of the contractile and protrusive stresses as a function of ρ_m and ρ_f, respectively, and are defined as $\eta_i(\rho_i) = \alpha_i \overline{\eta}_i + (1 - \alpha_i)\overline{\eta}_i \mathscr{H}(\rho_i - \overline{\rho}_i)$, where $\mathscr{H}$ is a smoothed-out Heaviside function, α_i and $\overline{\rho}_i$ are constants, the parameter $\overline{\eta}_i$ defines the maximum strength, and the index i represents m or f. The term δ_f in $\boldsymbol{\sigma}_{\text{prot}}$ cancels protrusive stresses in the surroundings of the obstacles. The repulsive stress $\boldsymbol{\sigma}_{\text{rep}} = \phi \eta_{\text{rep}} \delta_{\text{rep}} \nabla\phi \otimes \nabla\phi$ prevents the cell from penetrating the obstacles, where the parameter η_{rep} controls the strength of the stress and the function δ_{rep} annihilates $\boldsymbol{\sigma}_{\text{rep}}$ away from the obstacles. Eq. (24) also considers the surface tension of the membrane $\mathbf{F}_{\text{mem}} = -\gamma_\phi(\varepsilon \nabla^2 \phi - G'(\phi)/\varepsilon)\nabla\phi$, where γ_ϕ is the surface tension coefficient, and the cell-environment adhesion. The adhesive forces consist of a continuous drag force and a set of punctual adhesions modeled as springs, i.e., $\mathbf{F}_{\text{adh}} = -\varsigma \mathbf{u} + \sum_j \mathbf{F}^j_{\text{punct}}$ where ς is the drag coefficient and $\mathbf{F}^j_{\text{punct}}$ is the force exerted by the punctual adhesion j. More details on the forces acting on the actomyosin network may be found in [137]. The dynamics of the extracellular chemoattractant q is dictated by the equation

$$\frac{\partial(\varphi q)}{\partial t} = \nabla \cdot (D_q \varphi \nabla q) - r_q \varphi q + b_q \varphi S_q - k_q \delta_m q, \tag{25}$$

which accounts for the chemoattractant diffusion (D_q), a natural degradation (r_q), a source term $S_q(\mathbf{x})$ that localizes the production of chemoattractant to a particular region of space, with production rate b_q, and the uptake of q at the cell membrane with rate k_q. Note the use of the extracellular marker φ in Eq. (25). The chemoattractant binds to the membrane receptors, inducing the chemotactic response of

the cell [176]. We assume that the chemotactic response depends on the concentration of q along the membrane [110]. In particular, on the variations of q along the membrane (i.e., the gradient) and also on the average concentration (signaling noise hinders an accurate response for low values of q, while membrane receptor saturation blocks the response for high values of q [171]). Thus, we employ the parameters $\overline{q}$ (average concentration of q along the membrane) and $\overline{\nabla q}$ (characteristic gradient obtained from the values of q along the membrane) to bias the dynamics of the activator; more details in [137]. The activator a represents a generic signaling molecule that triggers actin polymerization. We propose the evolution equation

$$\frac{\partial(\delta_m a)}{\partial t} + \nabla\cdot(\delta_m a\mathbf{u}) = \nabla\cdot(D_a\delta_m\nabla a) - r_a\delta_m a + b_a\delta_m S_a, \tag{26}$$

which localizes the dynamics of a to the cell membrane through the marker δ_m; see Eq. (9). Eq. (26) takes into account activator diffusion (D_a), a natural decay (r_a), and a source term S_a with production rate b_a. The source term $S_a(\mathbf{x},t)$ accounts for the growth of actin protrusive structures (pseudopods in the case of amoeboid motion) in such a way that S_a drives a to $a_{\max} > 0$ at certain regions and interval times. We resort to a stochastic approach to define the function S_a. In particular, we employ probability distributions taken from experiments of spontaneous cell migration [29, 30]. The probability functions account for the spatial and temporal location of new pseudopods. In the case of chemotaxis, the probability functions for spontaneous migration are biased depending on the parameters $\overline{q}$ and $\overline{\nabla q}$; see the probability distribution of pseudopod extension for spontaneous (red) and chemotactic (green) migration in Fig. 9C-top. The chemotactic bias (Fig. 9C-bottom) is based on experimental observations [73,171,187]. More details about the parameters $\overline{q}$ and $\overline{\nabla q}$ and the algorithm to compute the function $S_a(\mathbf{x},t)$ may be found in [137]. In Sect. 5.1 we show some simulation results obtained from the model defined by Eqs. (16)–(26).

Under certain conditions, the number of equations that need to be solved in the previous approach can be reduced. The procedure to reduce the number of equations involves a simplification of the force balance equation [e.g., Eq. (24)] such that $\mathbf{u}$ can be obtained analytically and substituted into the phase-field equation [e.g., Eq. (4)]. The key assumption is neglecting the viscous stresses in the force balance equation (or approximating viscous forces by $-\kappa\mathbf{u}$ in 2D problems[5]). Some authors have resorted to this procedure to simulate rotational motion [37], keratocyte migration [166], and spontaneous amoeboid motion [9].

[5] In a Hele-Shaw cell [160], viscous forces can be approximated by $-\kappa\mathbf{u}$, where κ is a constant.

3.4 Collective cell migration

Models of collective migration have barely resorted to the phase-field method. There are some reasons that explain this fact. First, the computational cost of describing the motion of each cell with a different phase field. Second, since collective motion usually takes the form of confluent monolayers, other approaches (e.g, Vortex or Voronoi models; see Sect. 3.1) are computationally more efficient and have succeeded at simulating the dynamics of confluent monolayers. Finally, the phase-field description of cellular interactions such as cell-cell adhesion or cell-cell repulsion is not based on well-known approaches such as the Hertz contact theory or the Lennard-Jones potential. However, the phase-field method presents a couple of advantages: (i) direct implementation of the phase-field model in the case of non-confluent clusters of cells (Voronoi and vertex models cannot be directly used for non-confluent groups of cells) and (ii) an arbitrary cell geometry. These two ideas, in addition to the enhancement of the computational capabilities, have recently led to the development of new phase-field models for collective cell migration. The work proposed by Nonomura [142] is perhaps the first phase-field model of multicellular systems. The multicellular system dynamics is controlled by the functional $\mathscr{F}[\phi_1,\cdots,\phi_N] = \sum_n \mathscr{F}_n[\phi_n]$. A generic expression of the functional $\mathscr{F}_n$ may be written as

$$\begin{aligned}\mathscr{F}_n[\phi_n] &= \gamma_n\int_\Omega\left(\frac{G(\phi_n)}{\varepsilon}+\frac{\varepsilon}{2}|\nabla\phi_n|^2\right)\mathrm{d}\Omega \\ &+\frac{\kappa_n\varepsilon}{2}\int_\Omega\left(\nabla^2\phi_n-\frac{G'(\phi_n)}{\varepsilon^2}\right)^2\mathrm{d}\Omega+\frac{\lambda_n}{A_{n0}}\left(A_{n0}-\int_\Omega\phi_n^2\,\mathrm{d}\Omega\right)^2 \\ &+\sum_{m\neq n}\int_\Omega\frac{g_n}{2}\phi_n^\alpha\phi_m^\alpha\,\mathrm{d}\Omega-\sum_{m\neq n}\int_\Omega\frac{\omega_n\varepsilon^3}{4}|\nabla\phi_n|^\beta|\nabla\phi_m|^\beta\,\mathrm{d}\Omega,\end{aligned} \tag{27}$$

where the parameters α and β are positive integers and A_{n0} represents the cell volume $(\int_\Omega\phi_n^2\,\mathrm{d}\Omega)$ at the initial time. The functional $\mathscr{F}_n$ in Eq. (27) takes into account the surface tension (γ_n) and the bending energy (κ_n) of the membrane, cell volume conservation (λ_n), cell-cell repulsion (g_n), and cell-cell adhesion (ω_n). Note that the repulsive potential (g_n-term) avoids cell-cell overlapping. Nonomura also considers the influence of an external substance S (e.g., a chemoattractant) on the cell motion, which is included in the functional $\mathscr{F}_n$ through an expression similar to the repulsive and adhesive energies shown in Eq. (27) (the term that accounts for the influence of S has not been included in Eq. (27); more details in [142]). The membrane bending energy (κ_n-term) is usually disregarded because its influence on the cell's behavior is minimal. In Nonomura's model, the evolution equation for the phase field ϕ_n is expressed as $\partial\phi_n/\partial t = -\Gamma_n(\delta\mathscr{F}/\delta\phi_n)$. Nonomura [142] studied cell division, the 3D dynamics of monolayers (Fig. 10A), 2D cluster behavior (Fig. 10B), and chemotaxis. The formulation proposed in [142] permits to

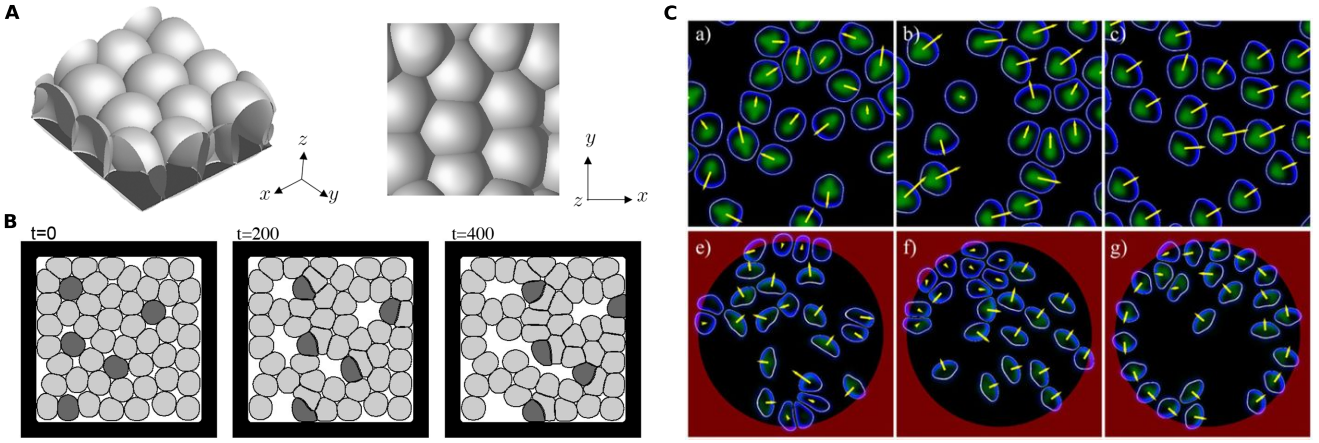

Fig. 10 Simulation results of collective migration. **A** Snapshot corresponding to a 3D simulation of a monolayer (top view on the right). Reproduced from [142]. **B** Time evolution of a 2D simulation of a cluster with two types of cells (dark and light gray). Reproduced from [142]. **C** Top row, time evolution of a cell cluster showing the emergence of translational collective migration. Bottom row, time evolution of a cell cluster in a circular domain showing the emergence of rotational collective motion. Arrows indicate the cell velocity, green regions indicate high adhesion, and blue regions correspond to high values of $|\mathbf{p}|$. Reproduced from [116].

study the behavior of cells with different properties (e.g., different stiffness, γ_n, size, A_{n0}, or adhesion, ω_n). An example of a collective migration model that does not couple the phase field ϕ_n with other unknowns is the model proposed in [94], which studies cell division and cell growth in closed domains. However, the phase field ϕ_n is usually coupled with other fields that account for constituents of the motile machinery. As done for individual cell migration (see Sect. 3.3), we divide collective phase-field models into those considering the polarization $\mathbf{p}$ and those considering the velocity $\mathbf{u}$.

Let us analyze first the models that couple ϕ_n with the polarization field $\mathbf{p}$, which accounts for the average orientation of the actin filaments. Löber and collaborators expanded the individual cell migration model presented in [115,206, 208] (see Sect. 3.3) and proposed a model for multicellular systems [116] that reproduces cell-cell collisions and the behavior of confluent and non-confluent cell clusters. The model identifies each cell with the phase field $\phi_n(\mathbf{x},t)$, while a single vector $\mathbf{p}(\mathbf{x},t)$ accounts for the polarization of the N cells. The evolution equation for the phase field is expressed as

$$\frac{\partial \phi_n}{\partial t}+\alpha \mathsf{A}\mathbf{p}\cdot\nabla\phi_n = D_\phi\nabla^2\phi_n-\phi_n(1-\phi_n)(\delta_p[\phi_n,\mathbf{p}]-\phi_n) - g\phi_n\sum_{m\neq n}\phi_m^2-\omega\nabla\phi_n\sum_{m\neq n}f(\nabla\phi_m), \tag{28}$$

where $\delta_p[\phi_n,\mathbf{p}]$ takes the same expression as in Eq. (12) and $f(x)=x/\sqrt{1+\zeta x^2}$, where ζ is a constant. Some of the terms on the right-hand side of Eq. (28) are similar to those in Nonomura's model, e.g., cell-cell repulsion and adhesion represented by the third and fourth terms, respectively. The coupling between ϕ_n and $\mathbf{p}$ appears in the advective term $(\alpha\mathsf{A}\mathbf{p}\cdot\nabla\phi_n)$ and the function δ_p. Note that Eq. (28) is equivalent to Eq. (12), but expanded with the cell-cell repulsive and adhesive terms. The evolution equation for the vector $\mathbf{p}$ is written as

$$\frac{\partial \mathbf{p}}{\partial t} = D_p\nabla^2\mathbf{p}-\beta_p\sum_n f(\nabla\phi_n)-\frac{\mathbf{p}}{\tau_1}-\frac{(1-\sum_n\phi_n^2)\mathbf{p}}{\tau_2} - \gamma(\sum_n\nabla\phi_n\cdot\mathbf{p})\mathbf{p}, \tag{29}$$

which is analogous to Eq. (13) but considering the N cells of the system rather than a single cell. The model proposed in [116] also considers the dynamics of adhesive bonds $\mathsf{A}(\mathbf{x},t)$, which is assumed to represent the adhesion of the N cells. The governing equation for A is written as

$$\frac{\partial \mathsf{A}}{\partial t} = D_\mathsf{A}\nabla^2\mathsf{A}+\sum_n\phi_n(a_0|\mathbf{p}|^2+a_{nl}\mathsf{A}^2)-\left[d(|\mathbf{d}|)+s\mathsf{A}^2\right]\mathsf{A}, \tag{30}$$

which is equivalent to Eq. (14). This approach (where a single field accounts for the dynamics of the N cells) is valid because all the terms in Eqs. (29) and (30) are local[6], the corresponding field vanishes outside each cell, and the cells do not overlap. However, a careful treatment of the terms including $\sum_n\phi_n$, $\sum_n\phi_n^2$, and $\sum_n\nabla\phi_n$ is required because some inaccuracies may arise in the neighborhood of cell-cell contacts. The model in [116] also considers the displacement $\mathbf{d}$ and the stress $\mathbf{T}$ of an elastic substrate. The definition of $\mathbf{d}$ and $\mathbf{T}$ is analogous to that explained in Sect. 3.3. The model defined by Eqs. (28)–(30) provides insight into cell-cell collisions (see Fig. 10C, top row) and the influence of cell-cell

[6] Eqs. (29) and (30) do not have any term that involves non-local computations associated to a single cell, such as, e.g., calculating integrals or distances.

adhesion in collective cell motility. The results also show the emergence of rotational motion in a multicellular closed system (see Fig. 10C, bottom row). A similar approach was developed in [127] to simulate cell-cell collisions and the dynamics of non-confluent cell clusters. The model in [127] may be thought of as an extension of the author's previous work [125]. Contrary to [116], the model proposed in [127] resorts to a set of N vectors $\mathbf{p}_n$ to account for the polarization of the N cells. This approach allows a better description of the cell dynamics with the caveat of a higher computational cost. Another model that takes into account the polarization $\mathbf{p}_n$ of each cell was proposed in [197], where the authors studied the behavior of confluent monolayers.

The model proposed by Palmieri and collaborators in [146] constitutes a prime example of a phase-field model of collective cell migration that utilizes velocity fields $\mathbf{u}_n$. The cell dynamics in [146] is based on a functional analogous to that defined in Eq. (27). The derivation of the phase-field equation is the same as shown in Eqs. (10) and (11). In addition to the velocity defined in Eq. (11), the model includes an active velocity $\mathbf{u}_{n,A}$, which is also assumed to be uniform in space. The active velocity $\mathbf{u}_{n,A}(t)$ accounts for the persistent random walk of the cells and is defined by using a stochastic approach. The model proposed in [146] was employed to study the role of the cellular stiffness in the dynamics of confluent monolayers. This model settled the bases for subsequent works that study the dynamics of confluent monolayers [139,149] and the role of cell elasticity [33] and cellular stresses [138] in collective migration.

We have extended the model presented in [146] to simulate chemotactic collective motion, where we consider paracrine (cell-to-cell) signaling; see Fig. 11. The cell dynamics in our model is derived from the functional $\mathscr{F}[\phi_1,\cdots,\phi_N] = \sum_n \mathscr{F}_n[\phi_n]$, where

$$\mathscr{F}_n[\phi_n] = \gamma_n \int_\Omega \left[\frac{30}{\varepsilon^2}\phi_n^2(1-\phi_n)^2 + |\nabla\phi_n|^2\right] \mathrm{d}\Omega \qquad (31)$$
$$+\frac{\lambda_n}{2A_{n0}}\left(A_{n0} - \int_\Omega \phi_n^2\,\mathrm{d}\Omega\right)^2 + g_n\frac{15}{\varepsilon^2}\int_\Omega \sum_{m\neq n}\phi_n^2\phi_m^2\,\mathrm{d}\Omega.$$

The energy functional in Eq. (31) is analogous to that in Eq. (27). In our model, we have neglected the membrane bending energy and the cell-cell adhesion; compare Eq. (31) with Eq. (27). In Eq. (31), γ_n is the surface tension coefficient, λ_n is a parameter controlling the strength of the cell volume conservation, A_{n0} represents the cell volume at the initial time, and g_n is a parameter setting the strength of the cell-cell repulsion. According to Eqs. (10) and (11), the evolution equation for the phase field takes the expression

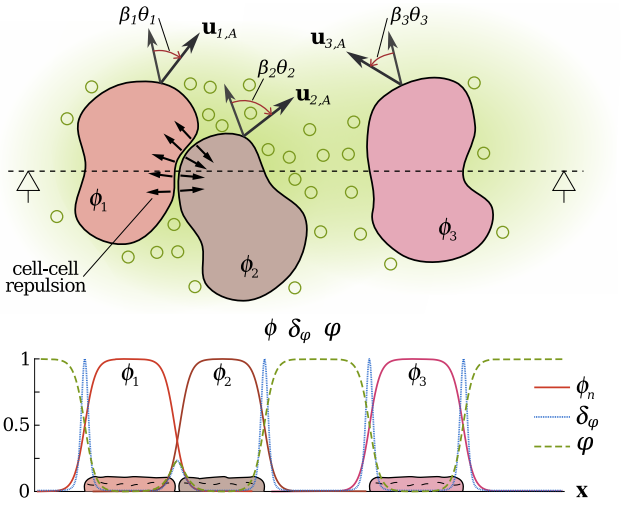

Fig. 11 Schematic representation of the phase-field model of collective chemotactic migration. Each cell is represented by a phase field ϕ_n. The chemoattractant released by the cells induces cell-cell attraction. The active velocity $\mathbf{u}_{n,A}$ is modified according to the chemotactic bias β_n (more details in Fig. 12). On the bottom, phase-field description of the cells (ϕ_n), the cells membrane (δ_φ), and the extracellular environment (φ).

$$\frac{\partial\phi_n}{\partial t} + \mathbf{u}_n\cdot\nabla\phi_n = -\Gamma_n\left[\gamma_n\frac{60}{\varepsilon^2}\phi_n(1-\phi_n)(1-2\phi_n)\right. \qquad (32)$$
$$\left. -2\gamma_n\nabla^2\phi_n - \frac{2\lambda_n}{A_{n0}}\phi_n\left(A_{n0} - \int_\Omega \phi_n^2\,\mathrm{d}\Omega\right) + g_n\frac{60}{\varepsilon^2}\sum_{m\neq n}\phi_n\phi_m^2\right],$$

where Γ_n is a constant. As done in [146], we consider two contributions to the velocity $\mathbf{u}_n(t)$, which is expressed as

$$\mathbf{u}_n = \mathbf{u}_{n,A} + \xi_n^{-1}\int_\Omega \frac{\delta\mathscr{F}}{\delta\phi_n}\nabla\phi_n\,\mathrm{d}\Omega$$
$$= \mathbf{u}_{n,A} + \frac{60g_n}{\xi_n\varepsilon^2}\int_\Omega \phi_n\nabla\phi_n\sum_{m\neq n}\phi_m^2\,\mathrm{d}\Omega, \qquad (33)$$

where ξ_n is a constant. Note that in Eq. (33), the γ_n and λ_n terms in $(\delta\mathscr{F}/\delta\phi_n)\nabla\phi_n$ may be shown to be zero integrating by parts. The second term in Eq. (33) arises from the phase-field formulation (more details in [146,200]) and represents the velocity resulting from cell-cell interactions. The first term ($\mathbf{u}_{n,A}$) accounts for the persistent random walk of each cell, which is biased by the extracellular chemoattractant $q(\mathbf{x},t)$. We assume that $\mathbf{u}_{n,A}$ is uniform in space. Below, we explain the stochastic description used to define $\mathbf{u}_{n,A}(t)$. Note that we model chemotaxis through the active velocity $\mathbf{u}_{n,A}$ rather than through the functional $\mathscr{F}$. We localize the chemoattractant dynamics to the extracellular environment by using the marker

$$\varphi(\mathbf{x},t) = 1 - \sum_n \phi_n(\mathbf{x},t), \qquad (34)$$

shown in Fig. 11. Note that in case of tight contact between cells, we may have a set of points $\mathbf{x}_C$ in the region of cell-cell contact such that $\sum_n \phi_n(\mathbf{x}_C,t) > 1$. In that case, we numerically set $\varphi(\mathbf{x}_C,t) = 0$, so that $\varphi(\mathbf{x},t) \in [0,1]$ for all $\mathbf{x}$. We define the function $\delta_\varphi(\varphi) = \frac{120}{\varepsilon^2}\varphi^2(1-\varphi)^2$ as a marker of the cells membrane; see Fig. 11. The governing equation for the chemoattractant q may be written as

$$\frac{\partial(\varphi q)}{\partial t} = \nabla\cdot(D_q\varphi\nabla q) - r_q\varphi q + b_q\delta_\varphi, \tag{35}$$

where we consider chemoattractant diffusion (D_q), degradation (r_q), and production caused by the cells themselves at a rate b_q. Following the rationale explained in Sect. 3.3 [see Eqs. (25) and (26)], we assume that the chemotactic response of each cell depends on the characteristic gradient $(\overline{\nabla q}_n)$ and average level $(\overline{q}_n)$ of chemoattractant along the membrane. The definition of the parameters $\overline{\nabla q}_n$ and $\overline{q}_n$ may be found in [137]. In the model proposed here, for each cell n, we divide the simulation time (t_f) in a set of I time intervals of length ΔT_n^i, such that $t_f = \sum_{i=1}^{I}\Delta T_n^i$. During each interval, we keep fixed the direction and magnitude of $\mathbf{u}_{n,A}$, hereinafter denoted as $\mathbf{u}_{n,A}^i$. Once a sub-interval has been completed, we need to provide the direction (α_n^i, where α_n^i is the angle between the vector $\mathbf{u}_{n,A}^i$ and the x-axis; see Fig. 12) and magnitude $(|\mathbf{u}_{n,A}^i|)$ of $\mathbf{u}_{n,A}^i$ for the next time interval, as well as the length of the interval (ΔT_n^i). Both α_n^i, $|\mathbf{u}_{n,A}^i|$, and ΔT_n^i are random variables given by the probability functions plotted in Figs. 9C and 12. Let us assume that we have just reached the final time of the interval i, in which the active velocity of the n-th cell was $\mathbf{u}_{n,A}^i$. The direction of $\mathbf{u}_{n,A}^i$ was α_n^i. The time interval $i+1$ will have duration ΔT_n^{i+1}, given by the probability function plotted in Fig. 12A, and the active velocity of the cell will be $\mathbf{u}_{n,A}^{i+1}$. The magnitude of $\mathbf{u}_{n,A}^{i+1}$ is given by the probability function plotted in Fig. 12B. The direction of the active velocity $\mathbf{u}_{n,A}^{i+1}$ is computed by adding a perturbation to the direction of $\mathbf{u}_{n,A}^{\star,i+1}$ which is the spontaneous (non-chemotactic) velocity of a cell that undergoes a persistent random walk. The direction of $\mathbf{u}_{n,A}^{\star,i+1}$ is a stochastic variable that we approximate from experimental data [30]. The direction of $\mathbf{u}_{n,A}^{\star,i+1}$ is denoted as $\alpha_n^{\star,i+1}$ and is defined as $\alpha_n^{\star,i+1} = \alpha_n^i + \Delta\alpha_n^\star$, where $\Delta\alpha_n^\star$ is given by the probability function plotted in Fig. 12C. Once we know the direction corresponding to spontaneous migration $(\alpha_n^{\star,i+1})$, we modify $\alpha_n^{\star,i+1}$ depending on the value of the parameters $\overline{\nabla q}_n$ and $\overline{q}_n$. If we denote the angle between $\mathbf{n}_{q,n}$ (the direction of $\overline{\nabla q}_n$; see [137]) and $\mathbf{u}_{n,A}^{\star,i+1}$ as θ_n^{i+1} (see Fig. 12D), the direction of the vector $\mathbf{u}_{n,A}^{i+1}$ accounting for chemotaxis is defined as $\alpha_n^{i+1} = \alpha_n^{\star,i+1} + \beta_n\theta_n^{i+1}$; see Fig. 12D. Here, β_n is the chemotactic bias that depends on the value of $|\overline{\nabla q}_n|$ and $\overline{q}_n$ according to the probability functions plotted in Fig. 9C (we only consider the *split* bias in the $\beta_{\overline{\nabla q}}$ plot). The procedure explained so far constitutes the stochastic description used to account for chemotaxis in our model of collective chemotaxis. We show results of our model in Sect. 5.2. Other authors have coupled the phase field ϕ_n and the velocity $\mathbf{u}_n$ with additional fields to study clusters with a small number of cells. For example, Camley and collaborators [37, 103] incorporated a pro-nucleation compound $\rho_n(\mathbf{x},t)$ and an inhibitor $I_n(\mathbf{x},t)$ into a phase-field model derived from a functional analogous to that shown in Eq. (31). As described in the Sect. 3.3, the authors obtained an explicit expression of $\mathbf{u}_n(\mathbf{x},t)$ from the force-balance equation and substituted $\mathbf{u}_n(\mathbf{x},t)$ into the phase-field equation. The incorporation of the fields ρ_n and I_n allowed to study persistent rotational motion, contact inhibition of locomotion, and cell-cell collisions on micropatterns [37, 103].

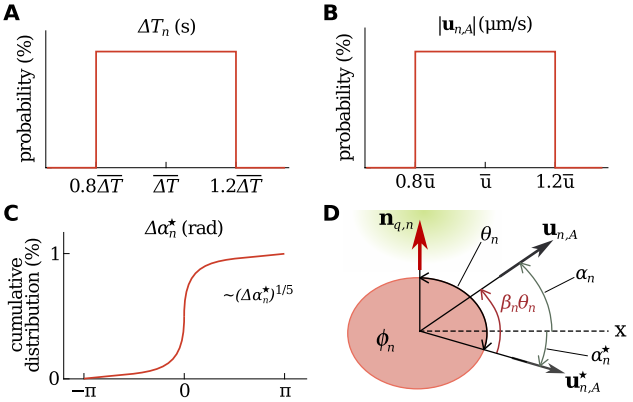

Fig. 12 Evaluation of the velocity $\mathbf{u}_{n,A}$. Probability distributions corresponding to: **A** the interval time (ΔT_n), **B** the velocity magnitude $(|\mathbf{u}_{n,A}|)$, and **C** the changes in the velocity direction corresponding to spontaneous migration $(\Delta\alpha_n^\star)$, where $\overline{\Delta T}$ and $\overline{u}$ are parameters. **D** Diagram showing the change in the velocity direction induced by chemotaxis. The direction of $\mathbf{u}_{n,A}$ results from rotating an angle $\beta_n\theta_n$ the direction of the velocity corresponding to spontaneous migration $(\mathbf{u}_{n,A}^\star)$. The angle $\beta_n\theta_n$ accounts for chemotaxis, where β_n is the chemotactic bias (see Fig. 9C) and θ_n is the angle between the spontaneous migration velocity $\mathbf{u}_{n,A}^\star$ and the chemotactic gradient direction $\mathbf{n}_{q,n}$. α_n (or $\alpha_n^\star$) is the angle between $\mathbf{u}_{n,A}$ (or $\mathbf{u}_{n,A}^\star$) and the x-axis.

Other phase-field theories have been used to model collective cell migration. For instance, the phase-field crystal model has been proposed to simulate cell-cell collisions and oscillatory motion in confined geometries [2], the dynamics of heterogeneous systems [3], and the dynamics of confluent monolayers [4]. In particular, [2,3] coupled the phase-field crystal model with a polar order parameter (somehow related to the cell velocity), while [4] employed a hybrid approach to simulate cell growth and mitosis in monolayers by using a single phase field.

4 Numerical simulation

In Sect. 3.2 we anticipated the main challenges we encounter when solving phase-field problems: localized regions of large gradients, equations that include higher-order derivatives, and dynamics with multiple time scales. In addition, collective cell migration models identify each cell with a different phase field, increasing the computational effort required to perform the simulations. Four types of numerical methods have been usually employed to solve phase-field problems of cell migration, namely, finite difference methods (FDM), spectral methods, finite element methods (FEM), and isogeometric analysis (IGA). Nevertheless, some works have resorted to other methods (e.g., the hybrid lattice Boltzmann method [181, 182]).

The FDM has been used in individual [38, 165, 166] and collective [103, 146] cell migration problems. For the time integration, the problem equations are usually solved with an explicit scheme. In some cases, the momentum conservation equation is solved with an implicit scheme [165] or a semi-implicit scheme [38]. Spectral or pseudo-spectral methods have been used in a number of works such as, e.g, [60, 116, 208]. The individual [206] and collective [116] cell migration models defined in Eqs. (12)–(15) and Eqs. (28)–(30), respectively, were solved using a quasi-spectral Fourier method. Finally, despite the challenges associated to solve phase-field models with FEM, some authors have resorted to FEM to solve their models [125, 126, 127].

We avoided most of the difficulties associated to the spatial discretization of the phase-field models by using isogeometric analysis (IGA) [89]. IGA is a generalization of finite elements that employs B-splines or NURBS (Non-uniform Rational B-splines) as basis functions. Classical finite element spaces use basis functions that are $\mathscr{C}^0$-continuous across element boundaries, making them unsuitable for higher-order problems using a standard Galerkin formulation. NURBS-based spaces can be constructed with arbitrary degrees of inter-element continuity for any spatial dimension. IGA exhibits higher-order accuracy, robustness, and the ability to preserve geometry during refinement. More details about IGA may be found in [20, 21, 55, 161, 162, 164].

Here, we describe the numerical methodology employed to solve the model defined by Eqs. (4), (16)–(26). Let us denote our fixed computational domain as Ω, whose boundary is Γ. We can assume periodic boundary conditions. Another option consists of assuming that the unknowns ϕ, ρ_m, ρ_f, and a vanish on Γ and $(\boldsymbol{\sigma}+\boldsymbol{\sigma}_{\text{myo}}+\boldsymbol{\sigma}_{\text{prot}}+\boldsymbol{\sigma}_{\text{rep}})\mathbf{n}=0$ and $\nabla q\cdot\mathbf{n}=0$ on Γ, where $\mathbf{n}$ is the unit outward normal to Γ. In both cases, the weak form of the problem takes the same expression. The weak form is obtained by multiplying the equations with weighting functions, integrating over the computational domain Ω, and integrating by parts. The weak form can be written as

$$\begin{aligned}
&\int_\Omega w_1\frac{\partial\phi}{\partial t}\,\mathrm{d}\Omega+\int_\Omega w_1\,\mathbf{u}\cdot\nabla\phi\,\mathrm{d}\Omega+\int_\Omega \Gamma_\phi\varepsilon\nabla w_1\cdot\nabla\phi\,\mathrm{d}\Omega\\
&\quad+\int_\Omega w_1\Gamma_\phi\frac{G'}{\varepsilon}\,\mathrm{d}\Omega-\int_\Omega\Gamma_\phi\varepsilon\nabla w_1\cdot\nabla\phi\,\mathrm{d}\Omega\\
&\quad-\int_\Omega w_1\frac{\Gamma_\phi\varepsilon}{|\nabla\phi|}\nabla\phi\cdot\nabla(|\nabla\phi|)\,\mathrm{d}\Omega=0,
\end{aligned}\tag{36}$$

$$\begin{aligned}
&\int_\Omega w_2\frac{\partial(\phi\rho_m)}{\partial t}\,\mathrm{d}\Omega-\int_\Omega\nabla w_2\cdot\mathbf{u}\phi\rho_m\,\mathrm{d}\Omega\\
&\quad+\int_\Omega D_m(\rho_f)\phi\nabla w_2\cdot\nabla\rho_m\,\mathrm{d}\Omega=0,
\end{aligned}\tag{37}$$

$$\begin{aligned}
&\int_\Omega w_3\frac{\partial(\phi\rho_f)}{\partial t}\,\mathrm{d}\Omega-\int_\Omega\nabla w_3\cdot\mathbf{u}\phi\rho_f\,\mathrm{d}\Omega\\
&\quad+\int_\Omega\Gamma_f\varepsilon_f^2\phi\nabla w_3\cdot\nabla\rho_f\,\mathrm{d}\Omega+\int_\Omega\Gamma_f w_3\phi\frac{\partial F_\rho}{\partial\rho_f}\,\mathrm{d}\Omega\\
&\quad-\int_\Omega\Gamma_f w_3\lambda_N\phi\,\mathrm{d}\Omega=0,
\end{aligned}\tag{38}$$

$$\begin{aligned}
&-\int_\Omega\nabla\mathbf{w}_4:\phi[\mu(\nabla\mathbf{u}+\nabla\mathbf{u}^T)+\lambda(\nabla\cdot\mathbf{u})\mathbf{I}]\,\mathrm{d}\Omega\\
&\quad-\int_\Omega\nabla\mathbf{w}_4:\phi\rho_m\eta_m\mathbf{I}\,\mathrm{d}\Omega+\int_\Omega\nabla\mathbf{w}_4:\phi\rho_f\eta_f\delta_f\nabla\phi\otimes\nabla\phi\,\mathrm{d}\Omega\\
&\quad-\int_\Omega\varsigma\mathbf{w}_4\cdot\mathbf{u}\,\mathrm{d}\Omega+\sum_j\mathbf{w}_4(\mathbf{x}^j)\cdot\mathbf{F}^j_{\text{punct}}\\
&\quad-\int_\Omega\gamma_\phi\,\mathbf{w}_4\cdot\nabla\phi(\varepsilon\nabla^2\phi-\frac{G'}{\varepsilon})\,\mathrm{d}\Omega\\
&\quad-\int_\Omega\nabla\mathbf{w}_4:\phi\eta_{\text{rep}}\delta_{\text{rep}}\nabla\phi\otimes\nabla\phi\,\mathrm{d}\Omega=0,
\end{aligned}\tag{39}$$

$$\begin{aligned}
&\int_\Omega w_5\frac{\partial(\varphi q)}{\partial t}\,\mathrm{d}\Omega+\int_\Omega D_q\varphi\nabla w_5\cdot\nabla q\,\mathrm{d}\Omega+\int_\Omega w_5 r_q\varphi q\,\mathrm{d}\Omega\\
&\quad-\int_\Omega w_5 b_q\varphi S_q\,\mathrm{d}\Omega+\int_\Omega w_5 k_q\delta_m q\,\mathrm{d}\Omega=0,
\end{aligned}\tag{40}$$

$$\begin{aligned}
&\int_\Omega w_6\frac{\partial(\delta_m a)}{\partial t}\,\mathrm{d}\Omega-\int_\Omega\nabla w_6\cdot\mathbf{u}\delta_m a\,\mathrm{d}\Omega\\
&\quad+\int_\Omega D_a\delta_m\nabla w_6\cdot\nabla a\,\mathrm{d}\Omega+\int_\Omega w_6 r_a\delta_m a\,\mathrm{d}\Omega\\
&\quad-\int_\Omega w_6 b_a\delta_m S_a\,\mathrm{d}\Omega=0,
\end{aligned}\tag{41}$$

where $\{w_i(\mathbf{x})\}_{i=1,\dots,6}$ are the weighting functions. Eqs. (36)–(41) are weak forms of Eqs. (4), (17), (20), (24)–(26), respectively. More details about the expression of the forces in Eq. (39) may be found in [137]. Note that we also need to determine λ_N and ρ_g from Eqs. (22) and (23) to close the problem. In the weak form, some of the terms become singular far from the cell and the cell membrane. We neglect the contribution of those terms in an appropriate region of the domain Ω (that is the reason why we do not cancel the

terms $\pm\Gamma_\phi \varepsilon \nabla w_1 \cdot \nabla\phi$ in Eq. (36)); see [136] for more details. A conforming discretization of the weak form requires basis functions which are at least $\mathscr{C}^1$-continuous across element boundaries. This is achieved by using IGA. We replace in the weak form the unknowns and the weighting functions with discrete approximations. For example, we replace $\phi(\mathbf{x},t)$ and $w_i(\mathbf{x})$ with

$$\phi^h(\mathbf{x},t) = \sum_A \phi^A(t) N^A(\mathbf{x}) \quad \text{and} \quad w_i^A(\mathbf{x}) = \sum_A w_i^A N^A(\mathbf{x}), \quad (42)$$

respectively. The basis functions N^A are splines with $\mathscr{C}^1$-global continuity, while the ϕ^A's are referred to as control variables. For the time integration, we employ a semi-implicit scheme based on the generalized-α method [51,93]. We treat implicitly all the terms of the residual, except those that require non-local computations, i.e., λ_N, ρ_g, and δ_{rep} (see [137] for more details). We use the Newton–Raphson method to solve the resulting non-linear system. In addition, we implemented a simple adaptive time stepping scheme that adjusts the time step as a function of the convergence of the Newton–Raphson solver. Note that the linear system that needs to be solved in the Newton–Raphson algorithm is ill-conditioned because most of the unknowns approach zero in large regions of the domain Ω. For instance, the activator concentration a tends to zero in regions far from the membrane. We improve the condition number of the system by replacing the appropriate rows of the tangent matrix by the corresponding rows of the identity matrix and replacing the associated elements of the residual vector by 0 (more details in [136]). A complete description of the numerical methodology introduced above may be found in [136,137]. By using this methodology, we solve the problem with a time step of $\sim 0.05\,\text{s}$, although smaller time steps are required during short time intervals of the simulation— as a reference, a cell travels a distance equivalent to its own diameter in $\sim 130\,\text{s}$.

5 Results

In this section we present some examples showing the capabilities of the phase-field method for cell migration problems. We include examples of individual and collective cell motion. We show 2D and 3D simulations of individual cell migration and 2D simulations of collective migration. We developed a code on top of the scientific libraries PETSc [17] and PetIGA [56] to perform the simulations corresponding to individual cell migration. To simulate collective cell motion, we developed a code based on the algorithm described in [26].

5.1 Individual cell migration

5.1.1 2D keratocyte migration

Keratocyte migration constitutes the simplest mode of cell motion on flat surfaces. In Sect. 2.3.6, we explained why many prominent experimental works of cell migration utilized keratocytes on planar substrates. For the same reasons, the first computational models of cell migration focused on keratocytes. Our model of keratocyte migration can be derived from the model for chemotactic amoeboid motion presented in Sect. 3.3 simply by disregarding the activator (a) and chemoattractant (q) dynamics and setting $I(a) = 0$ in Eq. (19). The model is able to reproduce spontaneous keratocyte migration, oscillatory and bipedal motion, and different keratocyte morphologies (see [136]).

In this section, we study the influence of the adhesion strength in our model. Note that we model cell-substrate adhesion as a set of punctual forces $\mathbf{F}^j_{\text{punct}}$ and a frictional drag force $\mathbf{F}_{\text{drag}} = -\varsigma\mathbf{u}$ where ς is the friction coefficient, such that $\mathbf{F}_{\text{adh}} = \mathbf{F}_{\text{drag}} + \sum_j \mathbf{F}^j_{\text{punct}}$; see Eq. (24). One of the open problems in continuum-scale modeling of cell migration is to propose a good model of cell-substrate adhesion. Here we show that the usual approach in which punctual adhesion forces are neglected and $\mathbf{F}_{\text{adh}} = -\varsigma\mathbf{u}$ may be inadequate and discuss potential alternatives. To motivate the discussion, we perform three simulations of spontaneous migration. In the first and second simulations we neglect punctual adhesion forces and take $\varsigma = 0.7$ and $20\,\text{pN}\,\text{s}\,\mu\text{m}^{-3}$, respectively. In the third simulation, we take $\varsigma = 0.7\,\text{pN}\,\text{s}\,\mu\text{m}^{-3}$ and incorporate punctual adhesion forces. We take $\overline{\eta}_m = 40\,\text{pN}\,\mu\text{m}$ and $\overline{\eta}_f = 1900\,\text{pN}\,\mu\text{m}^3$ in the three simulations. The values of the rest of the model parameters used in the simulations can be found in Table 1 in [136], except those related to the punctual adhesion forces which are listed in Table 2 in [137]. We use the computational domain $\Omega = [-L,L]^2$ with $L = 25\,\mu\text{m}$ and a mesh composed of 200 $\mathscr{C}^1$-continuous quadratic elements in each direction. We consider periodic boundary conditions. We use a fixed time step of $0.05\,\text{s}$. The initial conditions correspond to a circular cell of radius $9\,\mu\text{m}$ with uniform ρ_m and ρ_g densities inside the cell, such that $\rho_m(\mathbf{x},0) = \phi(\mathbf{x},0)$ and $\rho_g(\mathbf{x},0) = 1.1\phi(\mathbf{x},0)$. The initial ρ_f density is defined as $\rho_f(\mathbf{x},0) = \rho_f^{\text{pr}}\phi(\mathbf{x},0)$ if $x > x_c$ and $\rho_f(\mathbf{x},0) = \rho_f^{\text{pa}}\phi(\mathbf{x},0)$ elsewhere, where x_c is the x-coordinate of the cell's center and $\rho_f^{\text{pr}} = 1.5$ and $\rho_f^{\text{pa}} = 0.5$. Finally, we take $\mathbf{u}(\mathbf{x},0) = 0$. More details about the initial conditions may be found in [136]. The cell's motion is initiated due to the polarized (asymmetric) distribution of ρ_f in the initial condition.

We run the simulations until the cell displays a quasi-stationary motion, which is at time $\sim 100\,\text{s}$. The time evolution of the keratocyte with $\varsigma = 0.7\,\text{pN}\,\text{s}\,\mu\text{m}^{-3}$ and no punc-

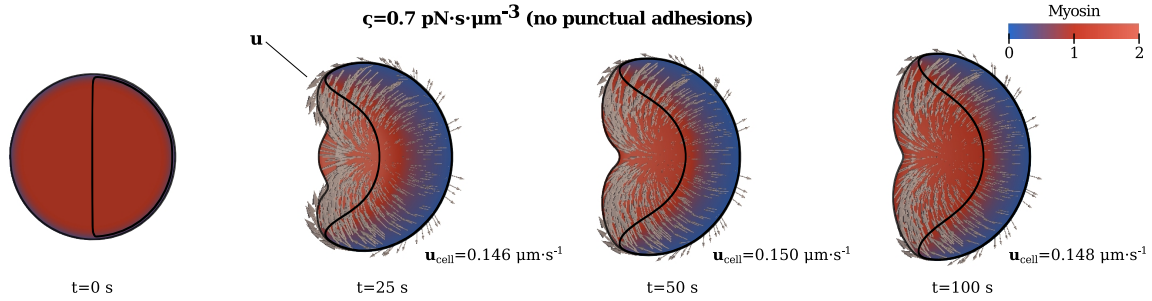

Fig. 13 2D keratocyte migration. Time evolution of a simulation with friction coefficient $\varsigma = 0.7\,\mathrm{pN\,s\,\mu m^{-3}}$ and no punctual adhesions. The plot shows the myosin density and actin velocity $\mathbf{u}$ (gray arrows) distributions at four different times. The solid black line delimits the lamellipodium. The velocity of the mass center of the cell $\mathbf{u}_{\mathrm{cell}}$ is indicated for each time. The cell achieves a stationary state at $t \approx 100\,\mathrm{s}$.

tual adhesions is shown in Fig. 13. We have plotted the myosin density and actin network velocity (gray arrows) distributions at $t = 0$, 25, 50, and 100 s. We have indicated the region occupied by the lamellipodium with a black solid line. In our model, the lamellipodium is represented by regions of higher ρ_f density. In Fig. 13, the black solid line identifies the points $\mathbf{x}$ such that $\rho_f(\mathbf{x},t) = (\rho_f^{\mathrm{pr}} + \rho_f^{\mathrm{pa}})/2$. We have also indicated the velocity of the mass center of the cell $\mathbf{u}_{\mathrm{cell}}(t)$. The results show a keratocyte with realistic morphodynamics. The cellular shape, the flow of the actin network (including the actin retrograde flow), the myosin distribution, the cell velocity ($\mathbf{u}_{\mathrm{cell}}$), and the region occupied by the lamellipodium are in good agreement with experiments (compare with [69,98]).

We next increase the cell-substrate adhesion strength. If punctual adhesions are neglected, adhesion strength is simply adjusted through the friction coefficient ς. In Fig. 14A we have plotted the simulation results of the keratocyte with $\varsigma = 20\,\mathrm{pN\,s\,\mu m^{-3}}$ and no punctual adhesions. Note that Fig. 14 displays the same format as Fig. 13, except for the arrows: gray arrows in Fig. 13 represent the velocity $\mathbf{u}$ distribution, while green arrows in Fig. 14 represent the punctual adhesion forces $\mathbf{F}^j_{\mathrm{punct}}$. Comparing Figs. 13 and 14A, we observe that the cell velocity $\mathbf{u}_{\mathrm{cell}}$ decreases as the adhesion strength (i.e., the value of ς) increases. The velocity $\mathbf{u}$ (not shown in Fig. 14A) is higher in the cell with low adhesion, which leads to differences in the shape of the lamellipodium and the cell. These facts are a consequence of modeling adhesion as a continuous frictional force: as adhesion increases (i.e., as friction increases) the velocity $\mathbf{u}$ decreases, modifying the cell morphology and reducing the cell velocity $\mathbf{u}_{\mathrm{cell}}$. This behavior does not agree with experimental observations [19], which show that cell velocity increases with adhesion until reaching an optimal level of adhesion. Since the continuous approach fails at reproducing the influence of cell-substrate adhesion, we next incorporate punctual adhesion forces and test the behavior of the model. In Fig. 14B we have plotted the time evolution of the keratocyte with $\varsigma = 0.7\,\mathrm{pN\,s\,\mu m^{-3}}$ and punctual adhesion forces (green arrows). For cells with the same friction coefficient, the incorporation of the punctual adhesions barely modifies the cell morphology (compare Figs. 13 and 14B) but increases the cell velocity $\mathbf{u}_{\mathrm{cell}} \sim 25\%$. The cell velocity $\mathbf{u}_{\mathrm{cell}}$ increases as the number of punctual adhesion increases and as the magnitude of the punctual adhesion forces increases (not shown in Fig. 14B). Punctual forces in Fig. 14B represent focal adhesions, which are formed at the leading edge and maturate as they translocate towards the cell's rear [49]. In our model, the punctual adhesions disengage before reaching the back of the cell. These results indicate that the continuous approach used to model cell-substrate adhesion cannot reproduce the experimentally-observed differences in keratocytes moving on substrates with different adhesion strength. The results also suggest that a discrete approach based on punctual forces, rather than a continuous frictional force, better captures the behavior of the cell-substrate adhesion. Many works have studied the dynamics of the integrin-mediated adhesion complex [49,69,96,205] and proposed different models [18,144] that may constitute the bases for future models of cell migration.

5.1.2 2D chemotactic amoeboid migration

In this section we present a 2D simulation of chemotactic amoeboid migration in a maze-like environment. The maze is formed by rigid walls; see the maze layout in Fig. 15. The simulation presented here illustrates the potential of the model described in Sect. 3.3 and allows us to study chemotactic amoeboid migration and the interaction between the cell, the environment (here, the maze), and the extracellular chemoattractant. We disregard the punctual adhesion forces. We consider a square computational domain of size 100 μm. The domain is meshed with 400 $\mathscr{C}^1$-continuous quadratic elements in each direction. We assume the non-periodic boundary conditions described in Sect. 4, which account for a domain whose boundaries allow for neither chemoattractant flow nor cell penetration. The initial conditions consist of a circular cell of radius 8 μm centered at point $(80,80)\,\mu\mathrm{m}$.

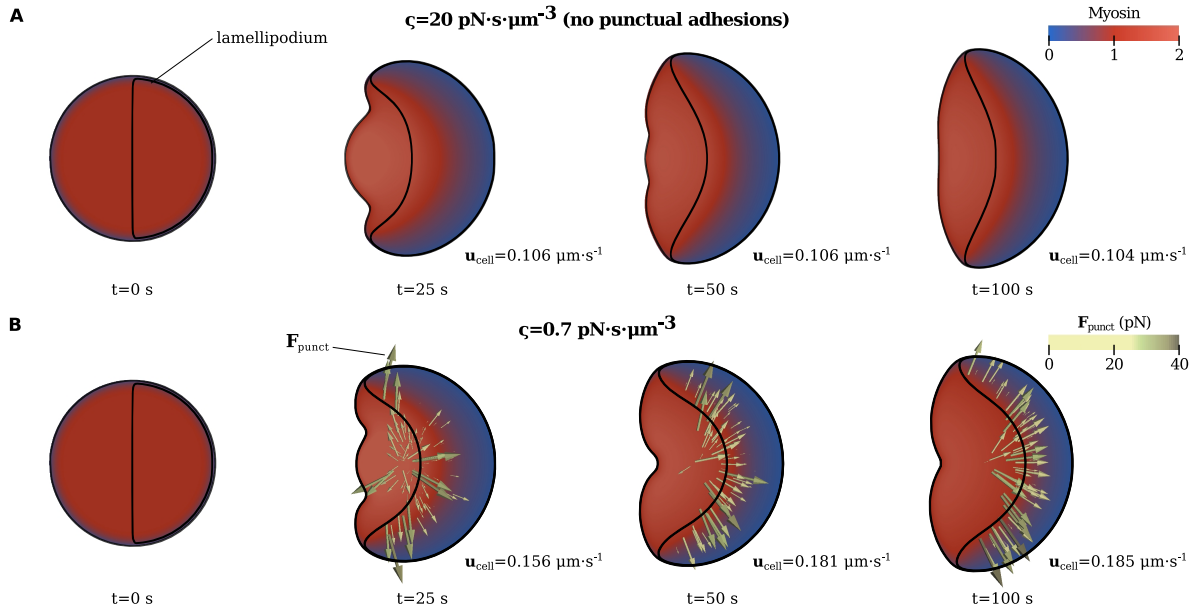

Fig. 14 Influence of adhesion strength on 2D keratocyte migration. Time evolution of two simulations with (**A**) $\varsigma = 20\,\mathrm{pN\,s\,\mu m^{-3}}$ and no punctual adhesions and (**B**) $\varsigma = 0.7\,\mathrm{pN\,s\,\mu m^{-3}}$ and punctual adhesions. The plot shows the myosin distribution and punctual adhesion forces $\mathbf{F}_{\mathrm{punct}}$ at four different times. The solid black line represents the lamellipodium. The velocity of the mass center of the cell $\mathbf{u}_{\mathrm{cell}}$ is indicated for each time. The cell achieves a stationary state at $t \approx 100\,\mathrm{s}$.

The cytosolic compounds at the initial time have a uniform density inside the cell and null density outside, such that $\rho_m(\mathbf{x},0)=\phi(\mathbf{x},0)$, $\rho_f(\mathbf{x},0)=\rho_f^{\mathrm{pa}}\phi(\mathbf{x},0)$, and $\rho_g(\mathbf{x},0)=1.1\phi(\mathbf{x},0)$, with $\rho_f^{\mathrm{pa}} = 0.5$. The chemoattractant, activator, and velocity vanish at the initial time. In addition, we consider a chemotactic source denoted as S_1 (yellow circle in Fig. 15), located at the point $(30,10)\,\mu\mathrm{m}$, which drives q to $q_{\max} = 250\,\mathrm{nM}$ in the neighborhood of that point (see the term S_q in Eq. (25); more details in [137]). The chemotactic source S_1 is active throughout the entire simulation. We took $D_q = 1000\,\mu\mathrm{m}^2\mathrm{s}^{-1}$. The remaining parameter values used in this simulation are listed in Table 1 in [137]. We use the adaptive time stepping scheme described in [137] with an initial time step of 0.05 s. We run the simulation until the cell reaches the chemotactic source, at $t \approx 1300\,\mathrm{s}$. In Fig. 15, we have plotted the computational domain and the cell at four different times ($t = 76$, 532, 694, and 1171 s). The main panel shows the numerical solution at $t = 76\,\mathrm{s}$ and the three rectangular insets show the numerical solution in the region occupied by the corresponding rectangle at $t = 532$, 694, and 1171 s. Fig. 15 shows the chemoattractant distribution outside the cell and the walls, the activator concentration along the cell membrane, and the F-actin distribution inside the cell. In addition, the yellow line represents the cell's path and the small crosses indicate the position of the cell's mass center at $t = 0$, 200, 400, 600, 800, 1000, and 1300 s. We have also indicated the cell's mass center (small black circle), the value of the parameters $\overline{q}$ and $|\overline{\nabla q}|$, and the direction of $\overline{\nabla q}$ ($\mathbf{n}_q$) at $t = 76$, 532, 694, and 1171 s. In Fig. 15 we can observe most of the features of our model. First, we succeed at reproducing amoeboid motion, which results from the balance between pseudopod extension and myosin-induced contraction (plots showing the accumulation of myosin at the cell's back may be found in [137] for a similar simulation). In Fig. 15, pseudopods are represented by regions of high F-actin density. The emergence of pseudopods is triggered by membrane patches of high activator concentration. The model is able to capture quick growth and retraction of pseudopods. Thus, the use of the phase-field methodology to model both the cell and the actin dynamics allows us to reproduce highly dynamic amoeboid motion that displays complex cell geometries. In Fig. 15, we can also see the influence of the chemoattractant in the motion of the cell. At the initial times, the cell is far from the chemotactic source. Hence, both $\overline{q}$ and $|\overline{\nabla q}|$ take low values, especially $|\overline{\nabla q}|$, which leads to a weak chemotactic response. This behavior can be observed at the initial times of the simulation ($t < 500\,\mathrm{s}$), where the cell exhibits a random-like walk. As the cell approaches the chemotactic source, the parameters $\overline{q}$ and $|\overline{\nabla q}|$ increase, enhancing the chemotactic response of the cell. In fact, the cell's path is nearly optimal for $t > 500\,\mathrm{s}$. Fig. 15 also shows the ability of our model to account for rigid obstacles that impede the motion of the cell. This fact allows us to simulate cell migration in complex and confined environments. But yet more interesting is the interplay between the obstacles, the cell, and the chemoattractant. Thanks to the use of the phase-field method, we can show a realistic picture of the chemoat-

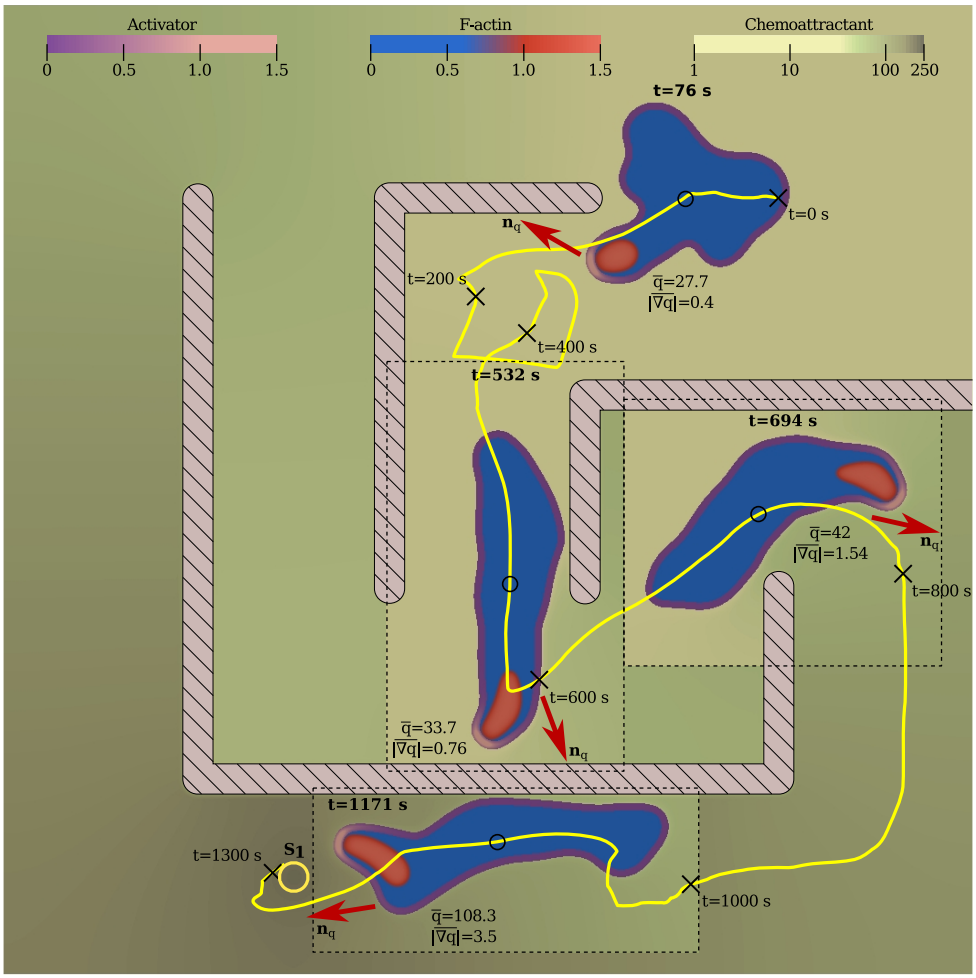

Fig. 15 2D chemotactic amoeboid migration. Activator (a), F-actin (ρ_f), and chemoattractant (q) distributions in a maze-like environment created with rigid walls (stripped grey regions). The main panel shows the distributions of a, ρ_f, and q at $t = 76$ s. The three rectangular insets show the distributions of a, ρ_f, and q in the neighborhood of the cell at $t = 532$, 694, and 1171 s. The yellow line represents the cell's path, while black crosses indicate the position of the cell's mass center at $t = 0$, 200, 400, 600, 800, 1000, and 1300 s. For the considered times (76, 532, 694, and 1171 s), we have indicated the values of the parameters $\overline{q}$ and $|\overline{\nabla q}|$ in nM and nM µm^{-1}, respectively, the direction of $\overline{\nabla q}$ ($\mathbf{n}_q$, red arrow), and the position of the cell's mass center (small circle).

tractant dynamics and, hence, chemotaxis. Both the cell and the obstacles impede the diffusion of chemoattractant, which originates situations as seen, e.g., at $t = 694$ s. At that time, the walls and the cell hinder the diffusion of chemoattractant towards the back of the cell. Thus, the chemoattractant concentration perceived by the cell's rear is lower than it would be in an open environment. Since the chemoattractant concentration is lower at the cell's back, the characteristic chemotactic gradient $|\overline{\nabla q}|$ increases. The increase in $|\overline{\nabla q}|$ induces a greater chemotactic response that leads to a more efficient chemotactic migration. In conclusion, our results suggest that taking into account the interplay between the cell, the cheomattractant, and the extracellular environment is crucial to study chemotaxis in complex environments.

5.1.3 3D migration in a fibrous environment

The 2D approach shown in the previous sections successfully captures the main features of cell migration on planar substrates. However, cells in the human body or in engineered matrices display a much more complex motion driven by mechanical and chemical interactions with the cell environment. Frequently, those cells migrate in the ECM. The ECM fiber density, orientation, and mechanical properties are key determinants of the ability of cells to migrate and the mode of motion displayed by the cells. Not only mechanical interactions, but also chemical interactions such as the ECM degradation induced by the cells or the ECM-mediated regulation of the signaling molecules dynamics are essential in cell migration. In this section, we consider a much simpler scenario that consists of a cell subjected to chemotaxis in

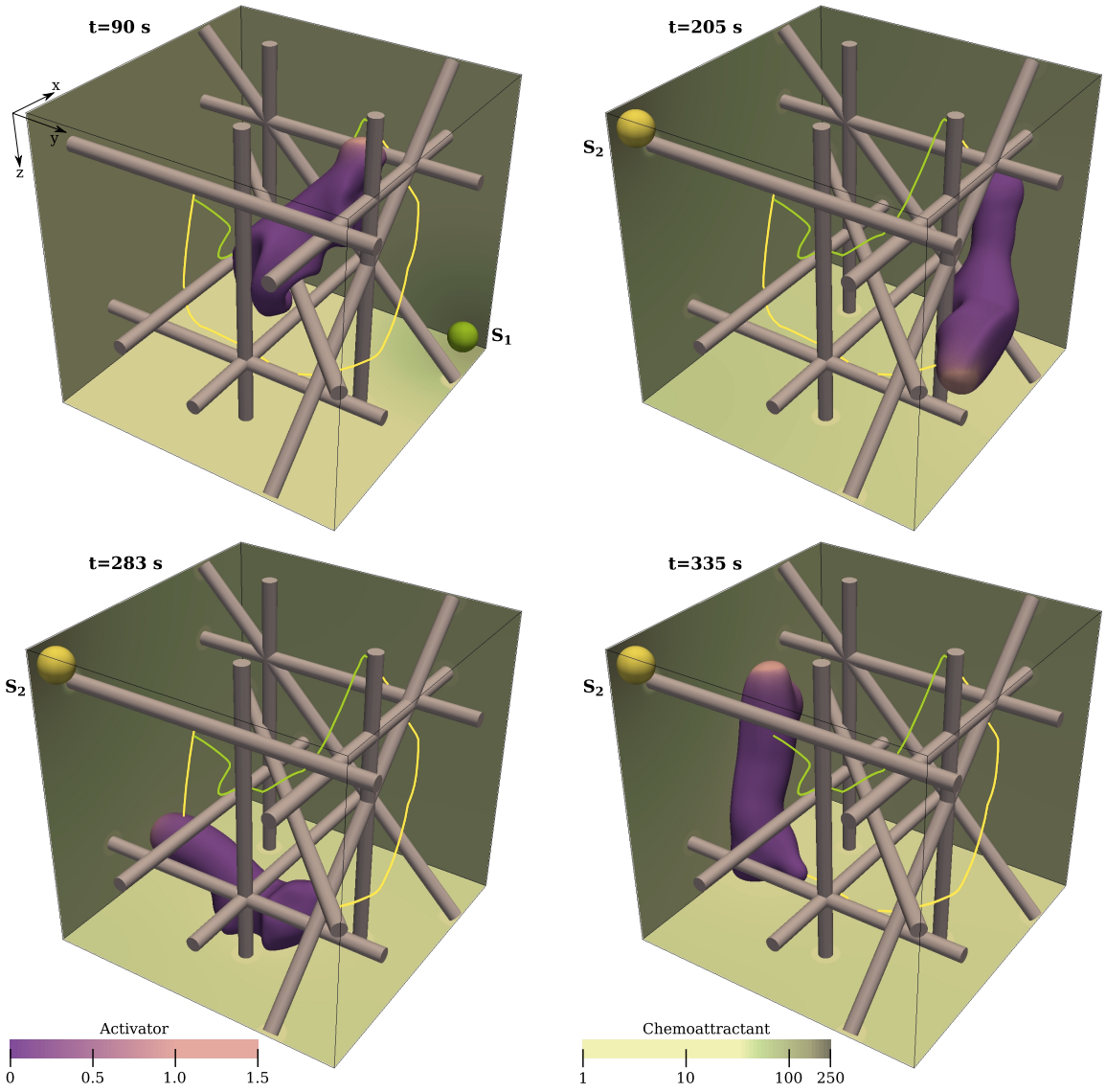

Fig. 16 3D migration in a fibrous environment. Activator concentration on the cell surface and chemoattractant concentration on three walls of the domain at $t = 90$, 205, 283, and 335 s. The radius of the fibers is slightly modified for visualization purposes. The green and yellow spheres represent the chemotactic sources S_1 and S_2, respectively, at the times in which they are active. The cell's path is divided into two segments according to the time intervals in which S_1 (green line) and S_2 (yellow line) are active.

a 3D fibrous environment, where the fibers are rigid cylinders; see the fibrous network layout in Fig. 16. A more precise picture of 3D migration would require elastic fibers, a more realistic geometry of the fibrous network, as well as a certain level of fiber degradation. However, the simple approach used here can provide insight into the interplay between the cell, the fibers, and the extracellular compounds. We solve the model for chemotactic amoeboid motion described in Sect. 3.3 on a cubic computational domain of size 38.4 µm. We mesh the computational domain with 128 $\mathscr{C}^1$-continuous quadratic elements in each direction. We consider the computational domain a closed system (see the non-periodic boundary conditions described in Sect. 4). We assume that punctual adhesions can only attach to the fibers, not to the walls of the domain. We use the adaptive time stepping scheme described in [137] with an initial time step of 0.1 s. The initial condition corresponds to a spherical cell of radius 7 µm centered at the point $(12,12,12)$ µm. The initial distributions of the cytosolic compounds are $\rho_m(\mathbf{x},0) = \phi(\mathbf{x},0)$, $\rho_f(\mathbf{x},0) = \rho_f^{\mathrm{pa}}\phi(\mathbf{x},0)$, and $\rho_g(\mathbf{x},0) = 0.9\phi(\mathbf{x},0)$, with $\rho_f^{\mathrm{pa}} = 0.5$. We assume that the activator, chemoattractant, and velocity vanish at the initial time. We account for chemotaxis by including the chemotactic source $S_q = S_1 + S_2$, where S_1 and S_2 are Gaussian functions in space centered at points $(36,36,36)$ and $(2,2,2)$ µm, respectively. S_1 drives q to $q_{\max,1} = 150$ nM, while S_2 drives q to $q_{\max,2} = 250$ nM. S_1 is ac-

tive in the time interval $(0,140)$ s, while S_2 in the interval $(140,350)$ s. We run the simulation until $t = 350$ s. The parameter values used in the simulation are listed in Tables 1 and 2 in [137]. In addition, we take $D_q = 400\,\mu\text{m}^2\text{s}^{-1}$. In Fig. 16, we plotted the simulation results at four different times. The chemoattractant concentration is plotted on three walls of the domain. The cell is represented by the surface defined by the points $\mathbf{x}$ such that $\phi(\mathbf{x},t) = 1/2$. The color of the cell surface represents the activator concentration. We have also plotted the chemotactic sources S_1 (green sphere) and S_2 (yellow sphere) at the times in which they are active. In Fig. 16, the green line represents the cell's path in the time interval in which S_1 is active, while the yellow line represents the cell's path in the interval time in which S_2 is active. The 3D simulation displays the same features of amoeboid motion as observed in 2D. That is, a highly dynamic motion with complex cell morphologies, which results from the balance between pseudopod extension and myosin contraction (myosin dynamics can be seen in Fig. 14 in [137]). Here, the cell acquires shapes even more intricate than in the 2D case due to the cell-fiber interaction. We were able, however, to reproduce those complex geometries without resorting to mesh refinement or small time steps (most of the time iterations in the simulation are performed with a time step of 0.1 s). The signaling parameters $|\overline{\nabla q}|$ and $\overline{q}$ are in a range of values (not shown in Fig. 16) that effectively bias the motion of the cell; see the cell's path in Fig. 16. In contrast to the 2D example (see Fig. 15), the cell's path in Fig. 16 is more erratic due to the fiber network geometry, which impedes a straight motion of the cell towards the chemotactic source. The complex and elongated geometries of the cell shown in Fig. 16 are favored by the presence of punctual adhesions at the cell's back (not shown in Fig. 16), which hinder the detachment of the cell's back from the fibers. In Fig. 16, the importance of the interplay between the chemoattractant dynamics, the fibers, and the cell is even more complex than in the 2D case. This fact is caused by the simplifications considered in the 2D example. However, the chemoattractant-ECM interaction in physiological conditions is more complex and plays a crucial role in cell migration. For instance, the chemoattractant diffusivity depends on the properties of the ECM. Also, there are some types of collective migration that involve paracrine and autocrine signaling [168]. The methodology proposed here can be used to accurately model the chemoattractant dynamics, including all the phenomena mentioned above. A more detailed description of the ECM requires to take into account the viscoelastic properties and the degradation of the ECM.

Symbol	Description	Value
ε	Phase-field interfacial length scale	$8\,\mu$m
γ_n	Surface tension coefficient	$5\,$pN
λ_n	Strength of cell volume constraint	$100\,\text{pN}\,\mu\text{m}^{-2}$
A_{n0}	Initial cell area[a]	$\pi 11.3^2\,\mu\text{m}^2$
g_n	Strength of cell-cell repulsion	$60\,$pN
Γ_n	Phase-field relaxation parameter	$0.5\,\mu\text{m}^2\text{pN}^{-1}\text{s}^{-1}$
ξ_n	Friction coefficient	$1500\,\text{pN}\,\text{s}\,\mu\text{m}^{-2}$
$\overline{\Delta T}$	Median of interval time	$50\,$s
$\overline{u}$	Median of active velocity	$0.2\,\mu\text{m}\,\text{s}^{-1}$
D_q	Chemoattractant diffusion coefficient	$140\,\mu\text{m}^2\text{s}^{-1}$
r_q	Chemoattractant decay rate	$0.1\,\text{s}^{-1}$

Table 1 Parameter values used in the simulations of collective cell migration.

[a] Note that Eq. (32) imposes cell volume conservation through the term $(A_{n0} - \int_\Omega \phi_n^2\,\mathrm{d}\Omega)$. The value of $\int_\Omega \phi^2\,\mathrm{d}\Omega$ corresponding to a circular cell of radius $12\,\mu$m and $\varepsilon = 8\,\mu$m is $\sim \pi 11.3^2\,\mu\text{m}^2$.

5.2 Collective cell migration

In this section we show simulation results corresponding to the phase-field model of chemotactic collective migration described in Sect. 3.4. The interaction between the cells and the environment (e.g., the signaling molecules dynamics) has been overlooked in most models of collective migration due to its complex implementation. The use of the phase-field method allows us to account for some of those interactions. In particular, we analyze cell co-attraction (i.e., paracrine signaling) in non-confluent multicellular systems. We study the dynamics of the chemically-driven co-attraction by means of two sets of simulations. In the first set, we study the influence of the initial intercellular separation. In the second set, we analyze the role played by the secretion rate of chemoattractant b_q; see Eq. (35). Note that in our model [see Eqs. (32)–(35)], we disregard cell-cell adhesion and account for the chemotactic response given by amoeboid cells [73, 187]. In addition, we consider the boundary of the domain as a wall that impedes the motion of the cells and the flux of chemoattractant (i.e., $\phi = 0$, $\nabla\phi \cdot \mathbf{n} = 0$, and $\nabla q \cdot \mathbf{n} = 0$ on the boundary, where $\mathbf{n}$ is the outward normal to the boundary). In this case, we follow [26] and use an explicit finite difference scheme to solve the system of equations. We use a fixed and uniform grid comprised of 300×300 nodes. The grid size is $\Delta x = \Delta y = 1\,\mu$m. Thus, we have a computational domain of $300 \times 300\,\mu\text{m}^2$. We use a time step $\Delta t_\phi = 0.01\,$s to update the phase field (ϕ_n) and a time step $\Delta t_q = 0.001\,$s to move forward the chemoattractant (q). To compute the dynamics of q, we assume that the time evolution of ϕ_n is linear during the time step Δt_ϕ. The initial configuration of the multicellular system corresponds to a square grid of 4×4 cells; see Fig. 17. The grid is located at the center of the domain. The grid size (i.e., the horizontal and vertical distance

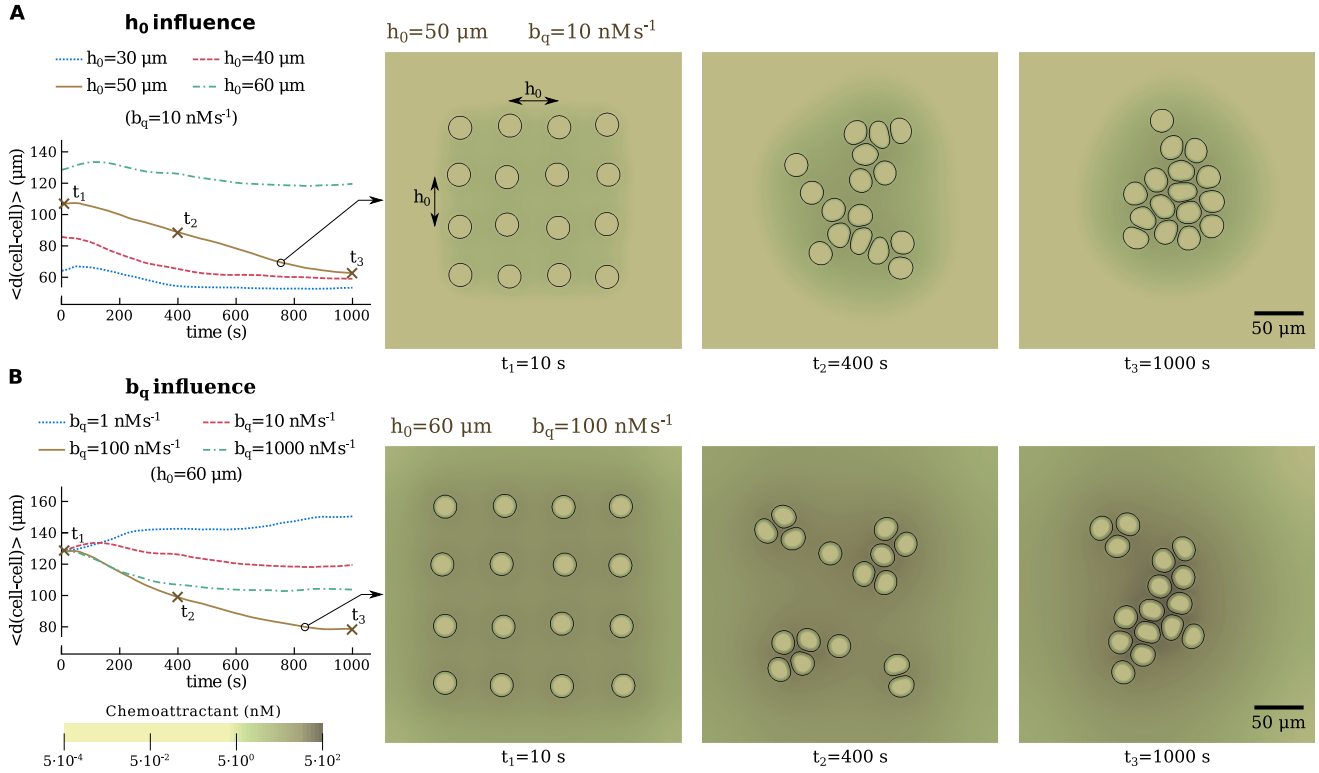

Fig. 17 Collective cell migration. Influence of (**A**) the initial intercellular separation and (**B**) the chemokine secretion rate b_q in the cell co-attraction process. **A** Influence of h_0 (intercellular separation in the initial configuration). Left, time evolution of the average cell-cell distance $\langle d \rangle$ for $h_0 = 30$, 40, 50, and 60 μm. Right, cells and chemoattractant distributions at $t = 10$, 400, and 1000 s for the case $h_0 = 50$ μm. **B** Influence of b_q. Left, time evolution of the average cell-cell distance $\langle d \rangle$ for $b_q = 1$, 10, 100, and 1000 nM s^{-1}. Right, cell and chemoattractant distributions at $t = 10$, 400, and 1000 s for the case $b_q = 100$ nM s^{-1}.

between consecutive cells) is denoted as h_0. The initial radius of the cells is 12 μm. The parameter values used in the simulations are listed in Table 1, except b_q and h_0, whose values vary for each simulation.

To analyze the influence of the intercellular separation, we performed four simulations with different values for h_0, while we kept fixed b_q. The simulation results are plotted in Fig. 17A. On the left, we plotted the time evolution of the average cell-cell distance $\langle d \rangle$ for $h_0 = 30$, 40, 50, and 60 μm. The parameter $\langle d \rangle$ can be defined as $\langle d \rangle = \frac{1}{N(N-1)} \sum_i^N \sum_{j \neq i}^N d_{ij}$, where N is the total number of cells and d_{ij} is the distance between the cells i and j. The parameter $\langle d \rangle$ indicates the level of aggregation of the system. The plot in Fig. 17A-left shows that clusters that are initially compact ($h_0 = 30$ μm) remain aggregated due to the chemotactic co-attraction. For intermediate values of h_0 (see the plot $h_0 = 50$ μm), the paracrine signal reaches the neighboring cells causing the aggregation of the system. However, systems with cells significantly distant (high values of h_0) are unable to aggregate because the paracrine signal perceived by the cells is weak; see the horizontal plot of $\langle d \rangle$ in the case $h_0 = 60$ μm. These results suggest the existence of a threshold of the intercellular distance for chemotactic co-attraction. In Fig. 17A-right, we plotted the cell (black solid lines) and the chemoattractant distributions at $t = 10$, 400, and 1000 s for the case $h_0 = 50$ μm. The snapshots show the aggregation of the cells. As the number of aggregated cells increases, the chemoattractant concentration becomes higher in the surroundings of the aggregate. Hence, the chemotactic gradient increases, which produces a positive feedback loop that enhances the aggregation process.

In Fig. 17B we show the influence of the chemokine secretion rate b_q. We performed four simulations with the same initial conditions ($h_0 = 60$ μm), but different values of b_q. In particular, we take $b_q = 1$, 10, 100, and 1000 nM s^{-1}. In Fig. 17B-left, we plotted the time evolution of the average cell-cell distance $\langle d \rangle$. The results show that both low and high values of b_q lead to slow aggregation (disaggregation in the case of $b_q = 1$ nM s^{-1}), while intermediate values of b_q induce fast aggregation. The slow aggregation for low values of b_q is caused by low chemoattractant concentrations that are unable to induce a chemotactic response in the cell. In the limit ($b_q = 0$ nM s^{-1}), the cells experience a persistent random walk that would lead, in most of the cases, to configurations of the multicellular system less aggregated than the initial configuration; see the case $b_q = 1$ nM s^{-1}. In the

case of high values of b_q, the slow aggregation is explained by the membrane receptor saturation [171]. Therefore, the results indicate that there is an optimal secretion rate for which the aggregation process is fastest. In Fig. 17B-right, we plotted three snapshots corresponding to the simulation with $b_q = 100\,\mathrm{nM\,s^{-1}}$. As in Fig. 17A-right, we observe an increase in the chemoattractant concentration as the number of aggregated cells increases. We can also observe the dynamics of the multicellular system. Initially, cells aggregate to form small clusters of 3-5 cells (see $t = 400\,\mathrm{s}$). Those small clusters subsequently aggregate to create bigger clusters, while some individual cells and small clusters may remain separated from the bigger clusters.

Since we have disregarded cell-cell adhesion, the aggregation process here is chemically-driven only. The incorporation of cell-cell adhesion into the model would lead to more tightly packed clusters, in which the detachment of individual cells would be hampered by the adhesive forces. In conclusion, in this section we have shown some of the features that make the phase-field method a powerful approach to computationally study multicellular systems. The phase-field method is essential to capture the interplay between the cells and the extracellular environment. Here, we have just considered a chemical interaction between the cells and the environment. The phase-field methodology permits a straightforward implementation of other phenomena such as, e.g., collective migration in confined and fibrous environments.

6 Conclusions

Cell migration is an active field of research due to its implications in key biological processes (e.g., cancer metastasis, tissue morphogenesis, or wound healing). Computational modeling has emerged as a tool used to further understand the mechanisms of cell migration and generate new hypotheses to be tested experimentally. In our opinion, cell migration models should (i) reproduce realistic cell morphodynamics, (ii) capture the dynamics/interactions of the main components of the cellular motile machinery, and (iii) resort to simple and fast numerical methods to solve the problem equations. The phase-field method has arisen as a new mathematical theory that achieves those goals in most types of cell migration. The main advantages of phase-field models lie in the description of moving domains and the location of evolution equations to moving volumes and surfaces without using moving meshes (see Sect. 3.2). In addition, the phase-field method permits a simple and straightforward treatment of the coupling between the intra- and extra-cellular elements that direct cell motion. This coupling enables the simulation of directed motion such as chemotaxis [137], haptotaxis [206], and durotaxis [115]. Despite the obvious utility of 2D models, the simulation of cell migration in more realistic environments requires a 3D approach. The aforementioned advantages of the phase-field method are particularly important in 3D because the classical moving boundary approach that requires compatible volume and surface meshes that evolve with time becomes very complicated algorithmically. As our computational capabilities grow, we also expect the phase-field method to be able to compete with classical vertex model for epithelial monolayers [10,68]. The phase-field approach may allow to extend vertex models to account for the interactions between the cells and the extracellular environment.

In the next few years we envision a significant growth of phase-field modeling approach for cell migration. The phase-field approach would be ideal to study, e.g., the influence on cell migration of other cell elements such as the nucleus or microtubules. New phase-field models of fluid-structure interaction [132] may also play a significant role in understanding the mechanical interaction of the cell with a deformable ECM. We also expect that phase-field theories will guide modeling efforts as more details about liquid-like assemblies at the intracellular level are discovered [169]. The phase-field models used in multiphase flows [32,79] have proven useful in modeling cell division [107], which usually plays an important role in migration of epithelial monolayers [13,151]. In conclusion, this is to our knowledge the first review on phase-field modeling of cell migration but we believe there are many more to come.

Compliance with Ethical Standards

Conflict of interest The authors declare that they have no conflict of interest.

References

1. Akiyama M, Sushida T, Ishida S, Haga H (2017) Mathematical model of collective cell migrations based on cell polarity. Development, growth & differentiation 59(5):471–490
2. Alaimo F, Praetorius S, Voigt A (2016) A microscopic field theoretical approach for active systems. New Journal of Physics 18(8):083,008. doi:10.1088/1367-2630/18/8/083008
3. Alaimo F, Voigt A (2018) Microscopic field-theoretical approach for mixtures of active and passive particles. Phys. Rev. E 98:032,605. doi:10.1103/PhysRevE.98.032605
4. Aland S, Hatzikirou H, Lowengrub J, Voigt A (2015) A mechanistic collective cell model for epithelial colony growth and contact inhibition. Biophysical Journal 109(7):1347 – 1357. doi:10.1016/j.bpj.2015.08.003
5. Alberts B, Johnson A, Lewis J, Raff M, Roberts K, Walter P. Molecular biology of the cell. Garland science (2007)
6. Allen SM, Cahn JW (1979) A microscopic theory for antiphase boundary motion and its application to antiphase domain coarsening. Acta Metallurgica 27(6):1085–1095. doi:10.1016/0001-6160(79)90196-2
7. Allena R, Aubry D (2012) Run-and-tumble or look-and-run? a mechanical model to explore the behavior of a migrating

amoeboid cell. Journal of theoretical biology 306:15–31. doi:10.1016/j.jtbi.2012.03.041
8. Allena R, Maini P (2014) Reaction–diffusion finite element model of lateral line primordium migration to explore cell leadership. Bulletin of mathematical biology 76(12):3028–3050. doi:10.1007/s11538-014-0043-7
9. Alonso S, Stange M, Beta C (2018) Modeling random crawling, membrane deformation and intracellular polarity of motile amoeboid cells. PloS one 13(8):e0201,977
10. Alt S, Ganguly P, Salbreux G (2017) Vertex models: from cell mechanics to tissue morphogenesis. Philosophical Transactions of the Royal Society B: Biological Sciences 372(1720):20150,520
11. Alt W, Dembo M (1999) Cytoplasm dynamics and cell motion: two-phase flow models. Mathematical biosciences 156(1):207–228. doi:10.1016/S0025-5564(98)10067-6
12. Anderson DM, McFadden GB, Wheeler AA (1998) Diffuse-interface methods in fluid mechanics. Annual review of fluid mechanics 30(1):139–165. doi:10.1146/annurev.fluid.30.1.139
13. Angelini TE, Hannezo E, Trepat X, Marquez M, Fredberg JJ, Weitz DA (2011) Glass-like dynamics of collective cell migration. Proceedings of the National Academy of Sciences 108(12):4714–4719
14. Antonopoulos M, Stamatakos G (2015) In silico neuro-oncology: Brownian motion-based mathematical treatment as a potential platform for modeling the infiltration of glioma cells into normal brain tissue. Cancer informatics 14:CIN–S19,341
15. Atakhani A, Mohammad-Rafiee F, Gholami A (2019) Influence of cross-linking and retrograde flow on formation and dynamics of lamellipodium. PloS one 14(3):e0213,810
16. Aubry D, Thiam H, Piel M, Allena R (2015) A computational mechanics approach to assess the link between cell morphology and forces during confined migration. Biomechanics and modeling in mechanobiology 14(1):143–157. doi:10.1007/s10237-014-0595-3
17. Balay S, Abhyankar S, Adams MF, Brown J, Brune P, Buschelman K, Dalcin L, Dener A, Eijkhout V, Gropp WD, Karpeyev D, Kaushik D, Knepley MG, May DA, McInnes LC, Mills RT, Munson T, Rupp K, Sanan P, Smith BF, Zampini S, Zhang H, Zhang H. PETSc Web page. `http://www.mcs.anl.gov/petsc` (2019)
18. Barnhart E, Lee KC, Allen GM, Theriot JA, Mogilner A (2015) Balance between cell- substrate adhesion and myosin contraction determines the frequency of motility initiation in fish keratocytes. Proceedings of the National Academy of Sciences 112(16):5045–5050
19. Barnhart EL, Lee KC, Keren K, Mogilner A, Theriot JA (2011) An adhesion-dependent switch between mechanisms that determine motile cell shape. PLoS biology 9(5):e1001,059. doi:10.1371/journal.pbio.1001059
20. Bazilevs Y, Calo VM, Cottrell JA, Evans JA, Hughes T, Lipton S, Scott MA, Sederberg TW (2010) Isogeometric analysis using t-splines. Computer Methods in Applied Mechanics and Engineering 199(5):229–263. doi:10.1016/j.cma.2009.02.036
21. Bazilevs Y, Michler C, Calo V, Hughes T (2010) Isogeometric variational multiscale modeling of wall-bounded turbulent flows with weakly enforced boundary conditions on unstretched meshes. Computer Methods in Applied Mechanics and Engineering 199(13):780–790. doi:10.1016/j.cma.2008.11.020
22. Bergert M, Chandradoss SD, Desai RA, Paluch E (2012) Cell mechanics control rapid transitions between blebs and lamellipodia during migration. Proceedings of the National Academy of Sciences 109(36):14,434–14,439. doi:10.1073/pnas.1207968109
23. Bi D, Yang X, Marchetti MC, Manning ML (2016) Motility-driven glass and jamming transitions in biological tissues. Physical Review X 6(2):021,011
24. Biben T, Kassner K, Misbah C (2005) Phase-field approach to three-dimensional vesicle dynamics. Physical Review E 72(4):041,921. doi:10.1103/PhysRevE.72.041921
25. Biben T, Misbah C (2003) Tumbling of vesicles under shear flow within an advected-field approach. Physical Review E 67(3):031,908
26. Biner SB. Programming phase-field modeling. Springer (2017)
27. Boas SE, Jiang Y, Merks RM, Prokopiou SA, Rens EG. Cellular potts model: Applications to vasculogenesis and angiogenesis. In: Probabilistic Cellular Automata, pp. 279–310. Springer (2018)
28. Borau C, Kim T, Bidone T, García-Aznar JM, Kamm RD (2012) Dynamic mechanisms of cell rigidity sensing: insights from a computational model of actomyosin networks. PLoS One 7(11):e49,174. doi:10.1371/journal.pone.0049174
29. Bosgraaf L, Van Haastert PJ (2009) Navigation of chemotactic cells by parallel signaling to pseudopod persistence and orientation. PloS one 4(8):e6842. doi:10.1371/journal.pone.0006842
30. Bosgraaf L, Van Haastert PJ (2009) The ordered extension of pseudopodia by amoeboid cells in the absence of external cues. PloS one 4(4):e5253. doi:10.1371/journal.pone.0005253
31. Bottino D, Mogilner A, Roberts T, Stewart M, Oster G (2002) How nematode sperm crawl. Journal of cell science 115(2):367–384
32. Boyer F, Lapuerta C (2006) Study of a three component cahn-hilliard flow model. ESAIM: Mathematical Modelling and Numerical Analysis 40(4):653–687
33. Bresler Y, Palmieri B, Grant M (2018) Effects of cell elasticity on the migration behavior of a monolayer of motile cells: Sharp interface model. arXiv preprint arXiv:1807.07836
34. Bueno J, Bazilevs Y, Juanes R, Gomez H (2017) Droplet motion driven by tensotaxis. Extreme Mechanics Letters 13:10–16. doi:10.1016/j.eml.2017.01.004
35. Cahn JW, Hilliard JE (1958) Free energy of a nonuniform system. i. interfacial free energy. The Journal of chemical physics 28(2):258–267. doi:10.1063/1.1744102
36. Camley BA, Rappel WJ (2017) Physical models of collective cell motility: from cell to tissue. Journal of Physics D: Applied Physics 50(11):113,002. doi:10.1088/1361-6463/aa56fe
37. Camley BA, Zhang Y, Zhao Y, Li B, Ben-Jacob E, Levine H, Rappel WJ (2014) Polarity mechanisms such as contact inhibition of locomotion regulate persistent rotational motion of mammalian cells on micropatterns. Proceedings of the National Academy of Sciences 111(41):14,770–14,775. doi:10.1073/pnas.1414498111
38. Camley BA, Zhao Y, Li B, Levine H, Rappel WJ (2013) Periodic migration in a physical model of cells on micropatterns. Physical review letters 111(15):158,102. doi:10.1103/PhysRevLett.111.158102
39. Camley BA, Zhao Y, Li B, Levine H, Rappel WJ (2017) Crawling and turning in a minimal reaction-diffusion cell motility model: Coupling cell shape and biochemistry. Physical Review E 95(1):012,401. doi:10.1103/PhysRevE.95.012401
40. Camley BA, Zimmermann J, Levine H, Rappel WJ (2016) Collective signal processing in cluster chemotaxis: Roles of adaptation, amplification, and co-attraction in collective guidance. PLoS computational biology 12(7):e1005,008
41. Campbell EJ, Bagchi P (2018) A computational model of amoeboid cell motility in the presence of obstacles. Soft matter 14(28):5741–5763
42. Cao Y, Karmakar R, Ghabache E, Gutierrez E, Zhao Y, Groisman A, Levine H, Camley BA, Rappel WJ (2019) Cell motility dependence on adhesive wetting. Soft Matter 15:2043–2050. doi:10.1039/C8SM01832D
43. Cardamone L, Laio A, Torre V, Shahapure R, DeSimone A (2011) Cytoskeletal actin networks in motile cells are critically self-organized systems synchronized by mechanical in-

teractions. Proceedings of the National Academy of Sciences 108(34):13,978–13,983. doi:10.1073/pnas.1100549108
44. Carlsson A (2011) Mechanisms of cell propulsion by active stresses. New journal of physics 13(7):073,009. doi:10.1088/1367-2630/13/7/073009
45. Casquero H, Bona-Casas C, Gomez H (2017) Nurbs-based numerical proxies for red blood cells and circulating tumor cells in microscale blood flow. Computer Methods in Applied Mechanics and Engineering 316:646–667. doi:10.1016/j.cma.2016.09.031
46. Chan CE, Odde DJ (2008) Traction dynamics of filopodia on compliant substrates. Science 322(5908):1687–1691. doi:10.1126/science.1163595
47. Charras G, Paluch E (2008) Blebs lead the way: how to migrate without lamellipodia. Nature reviews Molecular cell biology 9(9):730–736. doi:10.1038/nrm2453
48. Chen LQ (2002) Phase-field models for microstructure evolution. Annual review of materials research 32(1):113–140. doi:10.1146/annurev.matsci.32.112001.132041
49. Choi CK, Vicente-Manzanares M, Zareno J, Whitmore LA, Mogilner A, Horwitz AR (2008) Actin and α-actinin orchestrate the assembly and maturation of nascent adhesions in a myosin ii motor-independent manner. Nature cell biology 10(9):1039. doi:10.1038/ncb1763
50. Chugh P, Clark AG, Smith MB, Cassani DA, Dierkes K, Ragab A, Roux PP, Charras G, Salbreux G, Paluch EK (2017) Actin cortex architecture regulates cell surface tension. Nature Cell Biology 19(6):689–697. doi:10.1038/ncb3525
51. Chung J, Hulbert G (1993) A time integration algorithm for structural dynamics with improved numerical dissipation: the generalized-α method. Journal of applied mechanics 60(2):371–375. doi:10.1115/1.2900803
52. Cogan N, Guy RD (2010) Multiphase flow models of biogels from crawling cells to bacterial biofilms. HFSP journal 4(1):11–25. doi:10.2976/1.3291142
53. Coleman BD, Noll W (1963) The thermodynamics of elastic materials with heat conduction and viscosity. Archive for Rational Mechanics and Analysis 13(1):167–178. doi:10.1007/BF01262690
54. Cortese B, Palamà IE, D'Amone S, Gigli G (2014) Influence of electrotaxis on cell behaviour. Integrative Biology 6(9):817–830. doi:10.1039/C4IB00142G
55. Cottrell J, Hughes T, Reali A (2007) Studies of refinement and continuity in isogeometric structural analysis. Computer methods in applied mechanics and engineering 196(41):4160–4183. doi:10.1016/j.cma.2007.04.007
56. Dalcin L, Collier N, Vignal P, Crtes A, Calo V (2016) Petiga: A framework for high-performance isogeometric analysis. Computer Methods in Applied Mechanics and Engineering 308:151–181. doi:https://doi.org/10.1016/j.cma.2016.05.011
57. Danuser G, Allard J, Mogilner A (2013) Mathematical modeling of eukaryotic cell migration: insights beyond experiments. Annual review of cell and developmental biology 29:501–528. doi:10.1146/annurev-cellbio-101512-122308
58. Dawes AT, Edelstein-Keshet L (2007) Phosphoinositides and rho proteins spatially regulate actin polymerization to initiate and maintain directed movement in a one-dimensional model of a motile cell. Biophysical journal 92(3):744–768. doi:10.1529/biophysj.106.090514
59. Devreotes PN, Bhattacharya S, Edwards M, Iglesias PA, Lampert T, Miao Y (2017) Excitable signal transduction networks in directed cell migration. Annual Review of Cell and Developmental Biology 33:19.1–19.23. doi:10.1146/annurev-cellbio-100616-060739
60. Dreher A, Aranson IS, Kruse K (2014) Spiral actin-polymerization waves can generate amoeboidal cell crawling. New Journal of Physics 16(5):055,007. doi:10.1088/1367-2630/16/5/055007
61. van Drongelen R, Pal A, Goodrich CP, Idema T (2015) Collective dynamics of soft active particles. Physical Review E 91(3):032,706
62. Elliott CM, Stinner B, Venkataraman C (2012) Modelling cell motility and chemotaxis with evolving surface finite elements. Journal of The Royal Society Interface 9(76):3027–3044. doi:10.1098/rsif.2012.0276
63. Elosegui-Artola A, Oria R, Chen Y, Kosmalska A, Perez-Gonzalez C, Castro N, Zhu C, Trepat X, Roca-Cusachs P (2016) Mechanical regulation of a molecular clutch defines force transmission and transduction in response to matrix rigidity. Nature cell biology 18(5):540–566. doi:10.1038/ncb3336
64. Emmerich H. The diffuse interface approach in materials science: thermodynamic concepts and applications of phase-field models, vol. 73. Springer Science & Business Media (2003)
65. Escribano J, Sunyer R, Sánchez MT, Trepat X, Roca-Cusachs P, García-Aznar JM (2018) A hybrid computational model for collective cell durotaxis. Biomechanics and modeling in mechanobiology 17(4):1037–1052
66. Euteneuer U, Schliwa M (1984) Persistent, directional motility of cells and cytoplasmic fragments in the absence of microtubules. Nature 310(5972):58
67. Farhadifar R, Röper JC, Aigouy B, Eaton S, Jülicher F (2007) The influence of cell mechanics, cell-cell interactions, and proliferation on epithelial packing. Current Biology 17(24):2095–2104
68. Fletcher AG, Osterfield M, Baker RE, Shvartsman SY (2014) Vertex models of epithelial morphogenesis. Biophysical journal 106(11):2291–2304
69. Fournier MF, Sauser R, Ambrosi D, Meister JJ, Verkhovsky AB (2010) Force transmission in migrating cells. The Journal of cell biology 188(2):287–297. doi:10.1083/jcb.200906139
70. Frieboes HB, Jin F, Chuang YL, Wise SM, Lowengrub JS, Cristini V (2010) Three-dimensional multispecies nonlinear tumor growthii: tumor invasion and angiogenesis. Journal of theoretical biology 264(4):1254–1278
71. Friedl P, Wolf K (2003) Tumour-cell invasion and migration: diversity and escape mechanisms. Nature reviews. Cancer 3(5):362. doi:10.1038/nrc1075
72. Friedl P, Wolf K (2009) Plasticity of cell migration: a multiscale tuning model. The Journal of cell biology pp. jcb–200909,003. doi:10.1083/jcb.200909003
73. Fuller D, Chen W, Adler M, Groisman A, Levine H, Rappel WJ, Loomis WF (2010) External and internal constraints on eukaryotic chemotaxis. Proceedings of the National Academy of Sciences 107(21):9656–9659. doi:10.1073/pnas.0911178107
74. Gail MH, Boone CW (1970) The locomotion of mouse fibroblasts in tissue culture. Biophysical journal 10(10):980–993. doi:10.1016/S0006-3495(70)86347-0
75. Gamba A, de Candia A, Di Talia S, Coniglio A, Bussolino F, Serini G (2005) Diffusion-limited phase separation in eukaryotic chemotaxis. Proceedings of the National Academy of Sciences of the United States of America 102(47):16,927–16,932. doi:10.1073/pnas.0503974102
76. Giomi L, DeSimone A (2014) Spontaneous division and motility in active nematic droplets. Physical review letters 112(14):147,802
77. Gomez H, Bures M, Moure A (2019) A review on computational modelling of phase-transition problems. Philosophical Transactions of the Royal Society A 377(2143):20180,203
78. Gómez H, Calo VM, Bazilevs Y, Hughes TJ (2008) Isogeometric analysis of the cahn–hilliard phase-field model. Computer methods in applied mechanics and engineering 197(49):4333–4352. doi:10.1016/j.cma.2008.05.003
79. Gomez H, van der Zee KG (2018) Computational phase-field modeling. Encyclopedia of Computational Mechanics Second Edition pp. 1–35

80. González-Valverde I, García-Aznar JM (2018) Mechanical modeling of collective cell migration: An agent-based and continuum material approach. Computer Methods in Applied Mechanics and Engineering 337:246–262
81. Gracheva ME, Othmer HG (2004) A continuum model of motility in ameboid cells. Bulletin of mathematical biology 66(1):167–193. doi:10.1016/j.bulm.2003.08.007
82. Grimm H, Verkhovsky A, Mogilner A, Meister JJ (2003) Analysis of actin dynamics at the leading edge of crawling cells: implications for the shape of keratocyte lamellipodia. European Biophysics Journal 32(6):563–577. doi:10.1007/s00249-003-0300-4
83. van Haren J, Charafeddine RA, Ettinger A, Wang H, Hahn KM, Wittmann T (2018) Local control of intracellular microtubule dynamics by eb1 photodissociation. Nature cell biology 20(3):252
84. Hatzikirou H, Deutsch A (2008) Cellular automata as microscopic models of cell migration in heterogeneous environments. Current Topics in Developmental Biology 81:401–434. doi:10.1016/S0070-2153(07)81014-3
85. Hecht I, Skoge ML, Charest PG, Ben-Jacob E, Firtel RA, Loomis WF, Levine H, Rappel WJ (2011) Activated membrane patches guide chemotactic cell motility. PLoS computational biology 7(6):e1002,044. doi:10.1371/journal.pcbi.1002044
86. Heck T, Smeets B, Vanmaercke S, Bhattacharya P, Odenthal T, Ramon H, Van Oosterwyck H, Van Liedekerke P (2017) Modeling extracellular matrix viscoelasticity using smoothed particle hydrodynamics with improved boundary treatment. Computer Methods in Applied Mechanics and Engineering 322:515–540. doi:10.1016/j.cma.2017.04.031
87. Holmes WR, Edelstein-Keshet L (2012) A comparison of computational models for eukaryotic cell shape and motility. PLoS computational biology 8(12):e1002,793. doi:10.1371/journal.pcbi.1002793
88. Honda H. Geometrical models for cells in tissues. In: International review of cytology, vol. 81, pp. 191–248. Elsevier (1983)
89. Hughes TJ, Cottrell JA, Bazilevs Y (2005) Isogeometric analysis: Cad, finite elements, nurbs, exact geometry and mesh refinement. Computer methods in applied mechanics and engineering 194(39):4135–4195. doi:10.1016/j.cma.2004.10.008
90. Iglesias PA, Devreotes PN (2008) Navigating through models of chemotaxis. Current opinion in cell biology 20(1):35–40. doi:10.1016/j.ceb.2007.11.011
91. Iglesias PA, Devreotes PN (2012) Biased excitable networks: how cells direct motion in response to gradients. Current opinion in cell biology 24(2):245–253. doi:10.1016/j.ceb.2011.11.009
92. Insall RH (2010) Understanding eukaryotic chemotaxis: a pseudopod-centred view. Nature reviews. Molecular cell biology 11(6):453. doi:10.1038/nrm2905
93. Jansen KE, Whiting CH, Hulbert GM (2000) A generalized-α method for integrating the filtered navier–stokes equations with a stabilized finite element method. Computer methods in applied mechanics and engineering 190(3):305–319. doi:10.1016/S0045-7825(00)00203-6
94. Jiang J, Garikipati K, Rudraraju S (2019) A diffuse interface framework for modeling the evolution of multi-cell aggregates as a soft packing problem driven by the growth and division of cells. Bulletin of mathematical biology pp. 1–19
95. Joanny JF, Prost J (2009) Active gels as a description of the actin-myosin cytoskeleton. HFSP journal 3(2):94–104. doi:10.2976/1.3054712
96. Jurado C, Haserick JR, Lee J (2005) Slipping or gripping? fluorescent speckle microscopy in fish keratocytes reveals two different mechanisms for generating a retrograde flow of actin. Molecular biology of the cell 16(2):507–518. doi:10.1091/mbc.E04-10-0860
97. Keller EF, Segel LA (1971) Model for chemotaxis. Journal of theoretical biology 30(2):225–234. doi:10.1016/0022-5193(71)90050-6
98. Keren K, Pincus Z, Allen GM, Barnhart EL, Marriott G, Mogilner A, Theriot JA (2008) Mechanism of shape determination in motile cells. Nature 453(7194):475. doi:10.1038/nature06952
99. Kim MC, Whisler J, Silberberg YR, Kamm RD, Asada HH (2015) Cell invasion dynamics into a three dimensional extracellular matrix fibre network. PLoS computational biology 11(10):e1004,535
100. Kim T (2015) Determinants of contractile forces generated in disorganized actomyosin bundles. Biomechanics and modeling in mechanobiology 14(2):345–355. doi:10.1007/s10237-014-0608-2
101. Kim T, Hwang W, Kamm R (2009) Computational analysis of a cross-linked actin-like network. Experimental Mechanics 49(1):91–104. doi:10.1007/s11340-007-9091-3
102. Kockelkoren J, Levine H, Rappel WJ (2003) Computational approach for modeling intra-and extracellular dynamics. Physical Review E 68(3):037,702. doi:10.1103/PhysRevE.68.037702
103. Kulawiak DA, Camley BA, Rappel WJ (2016) Modeling contact inhibition of locomotion of colliding cells migrating on micropatterned substrates. PLOS Computational Biology 12(12):1–25. doi:10.1371/journal.pcbi.1005239
104. Kuusela E, Alt W (2009) Continuum model of cell adhesion and migration. Journal of mathematical biology 58(1-2):135. doi:10.1007/s00285-008-0179-x
105. Lämmermann T, Sixt M (2009) Mechanical modes of amoeboid-cell migration. Current opinion in cell biology 21(5):636–644. doi:10.1016/j.ceb.2009.05.003
106. Larripa K, Mogilner A (2006) Transport of a 1d viscoelastic actin–myosin strip of gel as a model of a crawling cell. Physica A: Statistical Mechanics and its Applications 372(1):113–123. doi:10.1016/j.physa.2006.05.008
107. Lee CF, Brangwynne CP, Gharakhani J, Hyman AA, Jülicher F (2013) Spatial organization of the cell cytoplasm by position-dependent phase separation. Physical review letters 111(8):088,101
108. Lee Y, Kouvroukoglou S, McIntire LV, Zygourakis K (1995) A cellular automaton model for the proliferation of migrating contact-inhibited cells. Biophysical journal 69(4):1284–1298. doi:10.1016/S0006-3495(95)79996-9
109. Levchenko A, Iglesias PA (2002) Models of eukaryotic gradient sensing: application to chemotaxis of amoebae and neutrophils. Biophysical journal 82(1):50–63. doi:10.1016/S0006-3495(02)75373-3
110. Levine H, Kessler DA, Rappel WJ (2006) Directional sensing in eukaryotic chemotaxis: a balanced inactivation model. Proceedings of the National Academy of Sciences 103(26):9761–9766. doi:10.1073/pnas.0601302103
111. Li X, Edwards M, Swaney KF, Singh N, Bhattacharya S, Borleis J, Long Y, Iglesias PA, Chen J, Devreotes PN (2018) Mutually inhibitory ras-pi (3, 4) p2 feedback loops mediate cell migration. Proceedings of the National Academy of Sciences 115(39):E9125–E9134
112. Li X, Lowengrub J, Rätz A, Voigt A (2009) Solving pdes in complex geometries: a diffuse domain approach. Communications in mathematical sciences 7(1):81
113. Lin SZ, Li B, Lan G, Feng XQ (2017) Activation and synchronization of the oscillatory morphodynamics in multicellular monolayer. Proceedings of the National Academy of Sciences 114(31):8157–8162
114. Liu WK, Liu Y, Farrell D, Zhang L, Wang XS, Fukui Y, Patankar N, Zhang Y, Bajaj C, Lee J, et al. (2006) Immersed finite element method and its applications to biological systems. Computer methods in applied mechanics and engineering 195(13):1722–1749. doi:10.1016/j.cma.2005.05.049
115. Löber J, Ziebert F, Aranson IS (2014) Modeling crawling cell movement on soft engineered substrates. Soft matter 10(9):1365–1373. doi:10.1039/C3SM51597D

116. Löber J, Ziebert F, Aranson IS (2015) Collisions of deformable cells lead to collective migration. Scientific reports 5:9172
117. Lorenzo G, Scott M, Tew K, Hughes T, Gomez H (2017) Hierarchically refined and coarsened splines for moving interface problems, with particular application to phase-field models of prostate tumor growth. Computer Methods in Applied Mechanics and Engineering 319:515–548. doi:10.1016/j.cma.2017.03.009
118. MacDonald G, Mackenzie JA, Nolan M, Insall R (2016) A computational method for the coupled solution of reaction–diffusion equations on evolving domains and manifolds: Application to a model of cell migration and chemotaxis. Journal of computational physics 309:207–226. doi:10.1016/j.jcp.2015.12.038
119. Mak M, Spill F, Kamm RD, Zaman MH (2016) Single-cell migration in complex microenvironments: mechanics and signaling dynamics. Journal of biomechanical engineering 138(2):021,004. doi:10.1115/1.4032188
120. Malet-Engra G, Yu W, Oldani A, Rey-Barroso J, Gov NS, Scita G, Dupré L (2015) Collective cell motility promotes chemotactic prowess and resistance to chemorepulsion. Current Biology 25(2):242–250
121. Malik-Garbi M, Ierushalmi N, Jansen S, Abu-Shah E, Goode BL, Mogilner A, Keren K (2019) Scaling behaviour in steady-state contracting actomyosin networks. Nature Physics 15:509–516
122. Mallet DG, De Pillis LG (2006) A cellular automata model of tumor–immune system interactions. Journal of theoretical biology 239(3):334–350. doi:10.1016/j.jtbi.2005.08.002
123. Marée AF, Grieneisen VA, Edelstein-Keshet L (2012) How cells integrate complex stimuli: the effect of feedback from phosphoinositides and cell shape on cell polarization and motility. PLoS computational biology 8(3):e1002,402. doi:10.1371/journal.pcbi.1002402
124. Marée AF, Hogeweg P (2001) How amoeboids self-organize into a fruiting body: multicellular coordination in dictyostelium discoideum. Proceedings of the National Academy of Sciences 98(7):3879–3883. doi:10.1073/pnas.061535198
125. Marth W, Praetorius S, Voigt A (2015) A mechanism for cell motility by active polar gels. Journal of The Royal Society Interface 12(107):20150,161
126. Marth W, Voigt A (2014) Signaling networks and cell motility: a computational approach using a phase field description. Journal of mathematical biology 69(1):91–112. doi:10.1007/s00285-013-0704-4
127. Marth W, Voigt A (2016) Collective migration under hydrodynamic interactions: a computational approach. Interface focus 6(5):20160,037
128. Meineke FA, Potten CS, Loeffler M (2001) Cell migration and organization in the intestinal crypt using a lattice-free model. Cell proliferation 34(4):253–266
129. Meinhardt H (1999) Orientation of chemotactic cells and growth cones: models and mechanisms. J Cell Sci 112(17):2867–2874
130. Mizuhara MS, Berlyand L, Aranson IS (2017) Minimal model of directed cell motility on patterned substrates. Physical Review E 96(5):052,408
131. Mogilner A, Manhart A (2018) Intracellular fluid mechanics: Coupling cytoplasmic flow with active cytoskeletal gel. Annual Review of Fluid Mechanics 50:347–370
132. Mokbel D, Abels H, Aland S (2018) A phase-field model for fluid–structure interaction. Journal of Computational Physics 372:823–840
133. Molina JJ, Yamamoto R (2019) Modeling the mechanosensitivity of fast-crawling cells on cyclically stretched substrates. Soft matter 15(4):683–698
134. Mori Y, Jilkine A, Edelstein-Keshet L (2008) Wave-pinning and cell polarity from a bistable reaction-diffusion system. Biophysical journal 94(9):3684–3697. doi:10.1529/biophysj.107.120824
135. Moure A, Gomez H (2016) Computational model for amoeboid motion: Coupling membrane and cytosol dynamics. Physical Review E 94(4):042,423. doi:10.1103/PhysRevE.94.042423
136. Moure A, Gomez H (2017) Phase-field model of cellular migration: Three-dimensional simulations in fibrous networks. Computer Methods in Applied Mechanics and Engineering 320:162–197. doi:10.1016/j.cma.2017.03.025
137. Moure A, Gomez H (2018) Three-dimensional simulation of obstacle-mediated chemotaxis. Biomechanics and modeling in mechanobiology 17(5):1243–1268
138. Mueller R, Yeomans JM, Doostmohammadi A (2019) Emergence of active nematic behavior in monolayers of isotropic cells. Physical Review Letters 122(4):048,004
139. Najem S, Grant M (2016) Phase-field model for collective cell migration. Physical Review E 93(5):052,405
140. Nava-Sedeño J, Hatzikirou H, Peruani F, Deutsch A (2017) Extracting cellular automaton rules from physical langevin equation models for single and collective cell migration. Journal of mathematical biology 75(5):1075–1100
141. Neilson MP, Veltman DM, van Haastert PJ, Webb SD, Mackenzie JA, Insall RH (2011) Chemotaxis: a feedback-based computational model robustly predicts multiple aspects of real cell behaviour. PLoS biology 9(5):e1000,618. doi:10.1371/journal.pbio.1000618
142. Nonomura M (2012) Study on multicellular systems using a phase field model. PloS one 7(4):e33,501
143. Novak IL, Gao F, Choi YS, Resasco D, Schaff JC, Slepchenko BM (2007) Diffusion on a curved surface coupled to diffusion in the volume: Application to cell biology. Journal of computational physics 226(2):1271–1290. doi:10.1016/j.jcp.2007.05.025
144. Oria R, Wiegand T, Escribano J, Elosegui-Artola A, Uriarte JJ, Moreno-Pulido C, Platzman I, Delcanale P, Albertazzi L, Navajas D, et al. (2017) Force loading explains spatial sensing of ligands by cells. Nature 552(7684):219
145. Otsuji M, Ishihara S, Kaibuchi K, Mochizuki A, Kuroda S, et al. (2007) A mass conserved reaction–diffusion system captures properties of cell polarity. PLoS computational biology 3(6):e108. doi:10.1371/journal.pcbi.0030108
146. Palmieri B, Bresler Y, Wirtz D, Grant M (2015) Multiple scale model for cell migration in monolayers: Elastic mismatch between cells enhances motility. Scientific reports 5:11,745
147. Palsson E, Othmer HG (2000) A model for individual and collective cell movement in dictyostelium discoideum. Proceedings of the National Academy of Sciences 97(19):10,448–10,453
148. Petitjean L, Reffay M, Grasland-Mongrain E, Poujade M, Ladoux B, Buguin A, Silberzan P (2010) Velocity fields in a collectively migrating epithelium. Biophysical journal 98(9):1790–1800
149. Peyret G, Mueller R, d'Alessandro J, Begnaud S, Marcq P, Mege RM, Yeomans J, Doostmohammadi A, Ladoux B (2018) Sustained oscillations of epithelial cell sheets. bioRxiv p. 492082
150. Potel MJ, Mackay SA (1979) Preaggregative cell motion in dictyostelium. Journal of cell science 36(1):281–309
151. Poujade M, Grasland-Mongrain E, Hertzog A, Jouanneau J, Chavrier P, Ladoux B, Buguin A, Silberzan P (2007) Collective migration of an epithelial monolayer in response to a model wound. Proceedings of the National Academy of Sciences 104(41):15,988–15,993
152. Provatas N, Elder K. Phase-field methods in materials science and engineering. John Wiley & Sons (2011)
153. Rapanan JL, Cooper KE, Leyva KJ, Hull EE (2014) Collective cell migration of primary zebrafish keratocytes. Experimental cell research 326(1):155–165
154. Reeves C, Winkler B, Ziebert F, Aranson IS (2018) Rotating lamellipodium waves in polarizing cells. Communications Physics 1(1):73
155. Rey R, Garcia-Aznar J (2013) A phenomenological approach to modelling collective cell movement in 2d. Biomechanics and modeling in mechanobiology 12(6):1089–1100. doi:10.1007/s10237-012-0465-9

156. Ribeiro F, Gómez-Benito M, Folgado J, Fernandes P, García-Aznar J (2017) Computational model of mesenchymal migration in 3d under chemotaxis. Computer methods in BiomeChaniCs and BiomediCal engineering 20(1):59–74. doi:10.1080/10255842.2016.1198784
157. Romanczuk P, Bär M, Ebeling W, Lindner B, Schimansky-Geier L (2012) Active brownian particles. The European Physical Journal Special Topics 202(1):1–162
158. Roussos ET, Condeelis JS, Patsialou A (2011) Chemotaxis in cancer. Nature reviews. Cancer 11(8):573. doi:10.1038/nrc3078
159. Rubinstein B, Fournier MF, Jacobson K, Verkhovsky AB, Mogilner A (2009) Actin-myosin viscoelastic flow in the keratocyte lamellipod. Biophysical journal 97(7):1853–1863. doi:10.1016/j.bpj.2009.07.020
160. Saffman PG, Taylor GI (1958) The penetration of a fluid into a porous medium or hele-shaw cell containing a more viscous liquid. Proceedings of the Royal Society of London. Series A. Mathematical and Physical Sciences 245(1242):312–329
161. Schillinger D, Dede L, Scott MA, Evans JA, Borden MJ, Rank E, Hughes TJ (2012) An isogeometric design-through-analysis methodology based on adaptive hierarchical refinement of nurbs, immersed boundary methods, and t-spline cad surfaces. Computer Methods in Applied Mechanics and Engineering 249:116–150. doi:10.1016/j.cma.2012.03.017
162. Schmidt R, Wüchner R, Bletzinger KU (2012) Isogeometric analysis of trimmed nurbs geometries. Computer Methods in Applied Mechanics and Engineering 241:93–111. doi:10.1016/j.cma.2012.05.021
163. Scianna M, Preziosi L, Wolf K (2013) A cellular potts model simulating cell migration on and in matrix environments. Mathematical Biosciences and Engineering 10(1):235–261. doi:10.3934/mbe.2013.10.235
164. Scott MA, Thomas DC, Evans EJ (2014) Isogeometric spline forests. Computer Methods in Applied Mechanics and Engineering 269:222–264. doi:10.1016/j.cma.2013.10.024
165. Shao D, Levine H, Rappel WJ (2012) Coupling actin flow, adhesion, and morphology in a computational cell motility model. Proceedings of the National Academy of Sciences 109(18):6851–6856. doi:10.1073/pnas.1203252109
166. Shao D, Rappel WJ, Levine H (2010) Computational model for cell morphodynamics. Physical review letters 105(10):108,104. doi:10.1103/PhysRevLett.105.108104
167. Shi C, Huang CH, Devreotes PN, Iglesias PA (2013) Interaction of motility, directional sensing, and polarity modules recreates the behaviors of chemotaxing cells. PLoS computational biology 9(7):e1003,122. doi:10.1371/journal.pcbi.1003122
168. Shields JD, Fleury ME, Yong C, Tomei AA, Randolph GJ, Swartz MA (2007) Autologous chemotaxis as a mechanism of tumor cell homing to lymphatics via interstitial flow and autocrine ccr7 signaling. Cancer cell 11(6):526–538
169. Shin Y, Brangwynne CP (2017) Liquid phase condensation in cell physiology and disease. Science 357(6357):eaaf4382
170. Song J, Kim D (2010) Three-dimensional chemotaxis model for a crawling neutrophil. Physical Review E 82(5):051,902
171. Song L, Nadkarni SM, Bödeker HU, Beta C, Bae A, Franck C, Rappel WJ, Loomis WF, Bodenschatz E (2006) Dictyostelium discoideum chemotaxis: threshold for directed motion. European journal of cell biology 85(9):981–989. doi:10.1016/j.ejcb.2006.01.012
172. Strychalski W, Copos CA, Lewis OL, Guy RD (2015) A poroelastic immersed boundary method with applications to cell biology. Journal of Computational Physics 282:77–97. doi:10.1016/j.jcp.2014.10.004
173. Strychalski W, Guy RD (2012) A computational model of bleb formation. Mathematical medicine and biology: a journal of the IMA 30(2):115–130. doi:10.1093/imammb/dqr030
174. Subramanian K, Narang A (2004) A mechanistic model for eukaryotic gradient sensing: spontaneous and induced phosphoinositide polarization. Journal of theoretical biology 231(1):49–67. doi:10.1016/j.jtbi.2004.05.024
175. Sunyer R, Conte V, Escribano J, Elosegui-Artola A, Labernadie A, Valon L, Navajas D, García-Aznar JM, Muñoz JJ, Roca-Cusachs P, et al. (2016) Collective cell durotaxis emerges from long-range intercellular force transmission. Science 353(6304):1157–1161
176. Swaney KF, Huang CH, Devreotes PN (2010) Eukaryotic chemotaxis: a network of signaling pathways controls motility, directional sensing, and polarity. Annual review of biophysics 39:265–289. doi:10.1146/annurev.biophys.093008.131228
177. Te Boekhorst V, Preziosi L, Friedl P (2016) Plasticity of cell migration in vivo and in silico. Annual review of cell and developmental biology 32:491–526. doi:10.1146/annurev-cellbio-111315-125201
178. Teigen KE, Li X, Lowengrub J, Wang F, Voigt A (2009) A diffuse-interface approach for modeling transport, diffusion and adsorption/desorption of material quantities on a deformable interface. Communications in mathematical sciences 4(7):1009. doi:10.4310/CMS.2009.v7.n4.a10
179. Theveneau E, Marchant L, Kuriyama S, Gull M, Moepps B, Parsons M, Mayor R (2010) Collective chemotaxis requires contact-dependent cell polarity. Developmental cell 19(1):39–53
180. Thiery JP (2002) Epithelial-mesenchymal transitions in tumour progression. Nature reviews. Cancer 2(6):442. doi:10.1038/nrc822
181. Tjhung E, Marenduzzo D, Cates ME (2012) Spontaneous symmetry breaking in active droplets provides a generic route to motility. Proceedings of the National Academy of Sciences 109(31):12,381–12,386
182. Tjhung E, Tiribocchi A, Marenduzzo D, Cates M (2015) A minimal physical model captures the shapes of crawling cells. Nature communications 6:5420. doi:10.1038/ncomms6420
183. Tozluoglu M, Tournier AL, Jenkins RP, Hooper S, Bates PA, Sahai E (2013) Matrix geometry determines optimal cancer cell migration strategy and modulates response to interventions. Nature cell biology 15(7):751. doi:10.1038/ncb2775
184. Trepat X, Wasserman MR, Angelini TE, Millet E, Weitz DA, Butler JP, Fredberg JJ (2009) Physical forces during collective cell migration. Nature physics 5(6):426
185. Truesdell C, Noll W. The non-linear field theories of mechanics. In: The non-linear field theories of mechanics, pp. 1–579. Springer (2004). doi:10.1007/978-3-662-10388-3_1
186. Valero C, Javierre E, García-Aznar J, Gómez-Benito M (2014) Nonlinear finite element simulations of injuries with free boundaries: application to surgical wounds. International journal for numerical methods in biomedical engineering 30(6):616–633
187. Van Haastert PJ (2010) A stochastic model for chemotaxis based on the ordered extension of pseudopods. Biophysical journal 99(10):3345–3354. doi:10.1016/j.bpj.2010.09.042
188. Van Haastert PJ, Devreotes PN (2004) Chemotaxis: signalling the way forward. Nature reviews. Molecular cell biology 5(8):626. doi:10.1038/nrm1435
189. Van Liedekerke P, Palm M, Jagiella N, Drasdo D (2015) Simulating tissue mechanics with agent-based models: concepts, perspectives and some novel results. Computational particle mechanics 2(4):401–444
190. Vedel S, Tay S, Johnston DM, Bruus H, Quake SR (2013) Migration of cells in a social context. Proceedings of the National Academy of Sciences 110(1):129–134
191. Vedula SRK, Leong MC, Lai TL, Hersen P, Kabla AJ, Lim CT, Ladoux B (2012) Emerging modes of collective cell migration induced by geometrical constraints. Proceedings of the National Academy of Sciences 109(32):12,974–12,979

192. Vermolen F, Gefen A (2013) A phenomenological model for chemico-mechanically induced cell shape changes during migration and cell–cell contacts. Biomechanics and modeling in mechanobiology pp. 1–23. doi:10.1007/s10237-012-0400-0
193. Vermolen F, Javierre E (2012) A finite-element model for healing of cutaneous wounds combining contraction, angiogenesis and closure. Journal of mathematical biology 65(5):967–996
194. Vicente-Manzanares M, Newell-Litwa K, Bachir AI, Whitmore LA, Horwitz AR (2011) Myosin iia/iib restrict adhesive and protrusive signaling to generate front–back polarity in migrating cells. The Journal of cell biology 193(2):381–396. doi: 10.1083/jcb.201012159
195. Vuong AV, Giannelli C, Jüttler B, Simeon B (2011) A hierarchical approach to adaptive local refinement in isogeometric analysis. Computer Methods in Applied Mechanics and Engineering 200(49-52):3554–3567
196. Wang X, Du Q (2008) Modelling and simulations of multicomponent lipid membranes and open membranes via diffuse interface approaches. Journal of mathematical biology 56(3):347–371
197. Wenzel D, Praetorius S, Voigt A (2019) Topological and geometrical quantities in active cellular structures. The Journal of chemical physics 150(16):164,108
198. Whitfield CA, Marenduzzo D, Voituriez R, Hawkins RJ (2014) Active polar fluid flow in finite droplets. The European Physical Journal E 37(2):8
199. Winkler B, Aranson IS, Ziebert F (2016) Membrane tension feedback on shape and motility of eukaryotic cells. Physica D: Nonlinear Phenomena 318:26–33
200. Wise SM, Lowengrub JS, Frieboes HB, Cristini V (2008) Three-dimensional multispecies nonlinear tumor growthi: model and numerical method. Journal of theoretical biology 253(3):524–543
201. Wu PH, Giri A, Sun SX, Wirtz D (2014) Three-dimensional cell migration does not follow a random walk. Proceedings of the National Academy of Sciences 111(11):3949–3954
202. Xi W, Sonam S, Saw TB, Ladoux B, Lim CT (2017) Emergent patterns of collective cell migration under tubular confinement. Nature communications 8(1):1517
203. Xu J, Vilanova G, Gomez H (2017) Full-scale, three-dimensional simulation of early-stage tumor growth: the onset of malignancy. Computer Methods in Applied Mechanics and Engineering 314:126–146. doi:10.1016/j.cma.2016.07.010
204. Yang L, Witten TM, Pidaparti RM (2013) A biomechanical model of wound contraction and scar formation. Journal of theoretical biology 332:228–248
205. Yao M, Goult BT, Klapholz B, Hu X, Toseland CP, Guo Y, Cong P, Sheetz MP, Yan J (2016) The mechanical response of talin. Nature communications 7:11,966
206. Ziebert F, Aranson IS (2013) Effects of adhesion dynamics and substrate compliance on the shape and motility of crawling cells. PloS one 8(5):e64,511
207. Ziebert F, Aranson IS (2016) Computational approaches to substrate-based cell motility. npj Computational Materials 2:16,019. doi:10.1038/npjcompumats.2016.19
208. Ziebert F, Swaminathan S, Aranson IS (2011) Model for self-polarization and motility of keratocyte fragments. Journal of The Royal Society Interface 9(70):1084–1092
209. Zimmermann J, Camley BA, Rappel WJ, Levine H (2016) Contact inhibition of locomotion determines cell–cell and cell–substrate forces in tissues. Proceedings of the National Academy of Sciences 113(10):2660–2665